Atmospheric Research 299 (2024) 107196

Contents lists available at ScienceDirect

Atmospheric Research

journal homepage: www.elsevier.com/locate/atmosres

Secondary droplet activation during condensational growth in convective clouds and its detection from satellites

Avichay Efraim [a,*], Ramon C. Braga [b], Daniel Rosenfeld [a], Oliver Lauer [c], Marco A. Franco [c,d,i], Leslie A. Kremper [c], Christopher Pöhlker [c], Meinrat O. Andreae [c,g,h], Cléo Q. Dias-Junior [j], Mira L. Pöhlker [c,e,f]

[a] Institute of Earth Sciences, The Hebrew University of Jerusalem, Jerusalem, Israel
[b] National Marine Research Centre, Southern Cross University, 2450 Coffs Harbour, Australia
[c] Multiphase Chemistry Department, Max Planck Institute for Chemistry, 55128 Mainz, Germany
[d] Institute of Physics, University of São Paulo, São Paulo 05508-900, Brazil
[e] Faculty of Physics and Earth Sciences, Leipzig Institute for Meteorology, University of Leipzig, 04103 Leipzig, Germany
[f] Atmospheric Microphysics Department, Leibniz Institute for Tropospheric Research, 04318 Leipzig, Germany
[g] Department of Geology and Geophysics, King Saud University, Riyadh, Saudi Arabia
[h] Scripps Institution of Oceanography, UCSD, La Jolla, CA, USA
[i] Research Centre for Greenhouse Gas Innovation (RCGI-POLI), University of São Paulo, Av. Professor Mello Moraes, 2231, Butantã, São Paulo 05508-030, Brazil
[j] Department of Physics, Federal Institute of Pará (IFPA), Av. Almirante Barroso, Belém 66093-020, PA, Brazil

ARTICLE INFO

Keywords:
Clouds
Remote sensing
Microphysics
Aerosols

ABSTRACT

By acting as cloud condensation nuclei (CCN), aerosol particles play a key role in the climate system. The CCN can be activated into cloud droplets at the cloud base (i.e., primary activation), or above it (i.e., secondary activation). This study shows the conditions required for secondary activation during the condensational growth phase in convective clouds. It also proposes a methodology for detecting this secondary activation from satellites. Using a spectral bin adiabatic parcel model, we simulate the vertical profile of cloud microphysical properties and demonstrate how different aerosol size distributions and updraft velocities greatly affect the secondary activation initiation and the cloud properties. The secondary activation slows down the cloud drop effective radius (r_e) growth rate with increasing height, and decreasing temperature (T), due to the relatively larger population of smaller droplets in the cloud parcel. Therefore, the vertical profile of r_e growth with height is slower than the adiabatic rate when the secondary activation occurs.

The proposed physical principle was verified by satellite-retrieved T-r_e profiles and adiabatic cloud drop number concentrations (N_d) over the Amazon region. The results obtained from this study can be utilized to identify the secondary droplet activation during the condensational growth phase, which can lead to an overestimation of the retrieved N_d as well as suppression of warm rain. This improves our knowledge and observational capabilities of the role of aerosol particles in the microphysics, dynamics, and precipitation behavior of convective clouds.

Plain text summary: Small particles serve as sites for cloud droplets' condensation at the cloud base (primary droplet activation) or above it (secondary activation). Once a droplet is activated at the cloud base, the surrounding water vapor condenses on it and the droplet grows - this is called condensational growth. The cloud droplet number concentrations (N_d) can be obtained by the satellite-retrieved vertical growth rate of droplet size in the condensational growth phase. However, new small droplets formed during this phase (i.e., secondary activation), might cause an overestimate in the retrieved N_d. This study presents the physical principle of secondary activation during condensational growth. Using a model, we simulate the condensational growth of aerosol particles, which act as cloud condensation nuclei (CCN), for different particle size distributions and thermodynamic conditions (i.e., vertical velocities). Our simulations show that secondary activation slows the cloud droplet growth rate with height due to the larger competition for the available water vapor promoted by the new drops. Comparisons between satellite-retrieved N_d of convective clouds and in-situ measurements show

* Corresponding author.
E-mail address: Avichay.Efraim@mail.huji.ac.il (A. Efraim).

https://doi.org/10.1016/j.atmosres.2023.107196
Received 18 October 2023; Received in revised form 14 December 2023; Accepted 16 December 2023
Available online 21 December 2023

that the satellite retrievals overestimate N_d when the secondary activation of droplets is neglected. Our findings improve the understanding of aerosols' role in the condensational growth of droplets in convective clouds.

1. Introduction

1.1. Background

The impacts of aerosols on clouds and climate are among the most significant uncertainties in assessing and modeling climate change (IPCC, 2013, 2021). Remote sensing techniques for studying aerosols and clouds allow worldwide monitoring and analysis of aerosol-cloud interactions (e.g., Rosenfeld and Lensky, 1998; Bréon et al., 2002; Rosenfeld et al., 2016; Grosvenor et al., 2018; Yang et al., 2021). Yet, analyzing aerosol and cloud characteristics with sufficient precision has remained a major challenge to quantify how cloud microstructure and the associated radiative properties respond to aerosol perturbations (e.g., Zhao et al., 2012; Efraim et al., 2020; Sayer et al., 2020).

The number concentration of cloud droplets (N_d; a list of abbreviations and symbols is given in Table 1) at the cloud base mainly depends on the activation spectrum of the aerosol particles that serve as cloud condensation nuclei (CCN) as a function of supersaturation (S) (Köhler, 1936; Twomey, 1959). The S rises when an air parcel is steadily cooled below the dew point due to the existing cloud base updraft (w_b). When S reaches a critical value (S_c), which is specific to the characteristics of a particular CCN, it is activated and grows into a droplet. As S increases, further activation of droplets occurs, and the already activated CCN continue to grow. Consequently, water vapor is removed by condensation at a steadily increasing rate, resulting in a slowing of the increase of S until the effect of condensation balances the growth of S due to cooling. Under the assumption of a fixed w_b, the maximum S at the cloud base (S_{max}) is reached within a small distance (a few to tens of meters) above the cloud base (Twomey, 1959; Rogers and Yau, 1996). Above the level of S_{max}, the existing droplets continue to grow, S starts to decrease, and no further CCN are activated. The N_d at the cloud base will then be determined by the number concentration of activated CCN (N_{CCN}) where $S_c \leq S_{max}$ (Twomey, 1959).

Table 1
List of abbreviations and notations.

Abbreviation/ notation	Description	Units
ACRIDICON-CHUVA	Aerosol, Cloud, Precipitation, and Radiation Interaction and Dynamics of Convective Cloud Systems - Cloud Processes of the Main Precipitation Systems in Brazil: A Contribution to Cloud Resolving Modeling and to the GPM (Global Precipitation Measurement)	–
ASD	Aerosol size distribution	cm^{-3}, nm
ATTO	Amazon Tall Tower Observatory	–
CCN	Cloud condensation nuclei	–
H_b	Cloud base height	km
LWC	Liquid water content	g/kg
LWC_a	Adiabatic liquid water content	g/kg
$M_{droplet}$	Mass of a single droplet	μg
N_a	The total particle number concentration	cm^{-3}, mg^{-1}
N_{CCN}	Number concentration of CCN	cm^{-3}, mg^{-1}
N_d	Number concentration of droplets	cm^{-3}, mg^{-1}
N_{da}	The adiabatic N_d (based on eq. 4 in Freud et al., 2011)	cm^{-3}, mg^{-1}
OLR	Outgoing longwave radiation	–
RWF	Rainwater fraction	–
r_e	The effective radius of the cloud droplet spectra	μm
r_v	The droplet mean-volume radius	μm
S	Supersaturation	%
SAZ	Secondary activation zone	–
SAZ_{coal}	Secondary activation above the coalescence phase	–
SAZ_{cond}	Secondary activation during the condensational growth	–
S_c	Critical supersaturation	%
S_{max}	Maximum supersaturation near cloud base	%
SMPS	Scanning Mobility Particle Sizer device	–
T	Temperature	°C
w	Updraft	ms^{-1}
w_b	Cloud base updraft	ms^{-1}

A common method for remote retrieval of N_d and N_{CCN} in growing convective towers is based on the growth of cloud drop effective radius (r_e) with height or decreasing temperature (T). This approach relies on aircraft observations showing that the measured r_e in different cloud depths above the cloud base increases almost as if the clouds were adiabatic. However, the cloud liquid water content (LWC) is mostly smaller than the adiabatic state (Freud et al., 2011; Braga et al., 2017). This pattern is caused by the nearly inhomogeneous mixing behavior of convective clouds with ambient air (Hill and Choularton, 1985; Paluch, 1986; Bower and Choularton, 1988; Brenguier, 1993; Brenguier et al., 2000; Burnet and Brenguier, 2007; Freud et al., 2008; Freud et al., 2011; Beals et al., 2015; Rosenfeld et al., 2016; Braga et al., 2017). Freud et al. (2011) showed that the cloud base N_d could be approximated by the ratio of adiabatic LWC (LWC_a) to the mass of a single droplet ($M_{droplet}$). The $M_{droplet}$ is calculated based on the mean-volume radius (r_v) where $r_v = \frac{r_e}{1.08}$ in an adiabatic process (Freud et al., 2011). Hereafter r_e and N_d in the adiabatic part are referred to as the adiabatic r_e and adiabatic N_d, respectively (Freud et al., 2011; Rosenfeld et al., 2016). Rosenfeld et al. (2014a) have shown that the T-r_e profiles can be retrieved by satellites and thus provide the capability of calculating the adiabatic N_d based on the assumption of adiabatic r_e and LWC_a. Using the cloud base height (H_b), w_b can be approximated based on the empirical relation $w_b = 0.9H_b$, where H_b is in km and w_b is in ms^{-1} (Zheng and Rosenfeld, 2015). Then, the estimated N_d and w_b are used to calculate S_{max} (Pinsky et al., 2012), where N_d is, by definition, N_{CCN} at S_{max}. Rosenfeld et al. (2016) combined all these considerations into a method to retrieve cloud base N_d and S_{max} by satellite, which is essentially the $N_{CCN}(S)$, with an accuracy of ±30%.

However, as pointed out earlier, N_d and N_{CCN} can only be retrieved from vertical T-r_e profiles as long as the r_e behaves adiabatically. The layers of the cloud where r_e is nearly adiabatic are where the condensation process dominates the cloud droplets' growth above the level of S_{max} close to the cloud base and below the level where the coalescence process dominates (i.e., for $r_e < 14$ μm (Rosenfeld et al., 2006)). Droplet coalescence increases the growth rate of r_e with decreasing T beyond the adiabatic condensational growth rate. The condensation phase of the cloud and its role in the calculation of N_d will be further described in Section 1.3.

1.2. Secondary activation zone

The process of activating cloud droplets well above the cloud base (above the height of S_{max}) is referred to herein as secondary activation, as opposed to the primary activation of droplets at the cloud base. Secondary activation might occur in two ways:

(1) When entrained particles from the cloud's lateral and/or top boundaries get activated as their characteristic S_c is lower than the actual S they experience in the cloud, which is smaller than S_{max}.
(2) When S above the cloud base exceeds the S_{max}. This can occur either when droplet coalescence reduces the integrated droplets' surface area available for condensation, which decreases the

condensation rate and increases S (Efraim et al., 2022), or when there is an increase in updraft (w), which increases S due to a higher cooling rate. As a result, particles, that were not activated at the cloud base because their S_c was greater than S_{max}, can now be activated into cloud droplets at the current elevated S.

Both mechanisms will reduce the observed r_e with decreasing T, due to the presence of a significant number of smaller droplets in an environment of fewer larger drops, where the newly activated droplets can dominate the r_e, as shown by several in-cloud aircraft campaigns (Warner, 1969; Paluch and Knight, 1984; Paluch and Baumgardner, 1989; Prabha et al., 2011; Braga et al., 2017; Bera et al., 2022). The secondary activation process might have an important impact on climate. The released latent heat from the activation of the new cloud droplets above the cloud base increases the buoyancy and further invigorates the cloud towards the tropopause (Khain et al., 2012; Fan et al., 2018). This invigoration may lead to more extensive and colder anvils in the form of cirrus clouds (Fan et al., 2013; Pan et al., 2021). These clouds efficiently absorb outgoing longwave radiation (OLR) and marginally reflect the incoming sunlight (Stephens et al., 1990). Therefore, during the day they might not have a large albedo, but they do absorb most of the OLR during day and night, eventually resulting in a positive radiative forcing and warming effect (Slingo and Slingo, 1988; Cotton et al., 2011). Moreover, the evaporation of ice crystals from these anvils enriches the upper troposphere with water vapor, which is a strong greenhouse gas (Price, 2000). Therefore, it will likely strengthen the positive radiative forcing.

The vertical microphysical zone in the cloud where the secondary activation occurs is defined as the "secondary activation zone" (*SAZ*). Efraim et al. (2022) presented a method to identify the post-coalescence *SAZ* along with other microphysical zones from satellite observations. This method analyses the T-r_e profile and divides the cloud into different microphysical zones based on the growth rate of r_e with decreasing T (dr_e/dT) compared to the adiabatic growth rate of r_e:

(1) condensational growth - r_e growth rate is similar to an adiabatic r_e curve originating at the cloud base;
(2) coalescence - the growth rate of r_e exceeds the adiabatic growth rate;
(3) rainout - a moderation of the growth rate of r_e after coalescence;
(4) secondary activation – a negative growth rate of r_e;
(5) mixed-phase of ice and water – a rapid regrowth of r_e above the subzero temperatures; and.
(6) glaciation – where the indicated r_e reaches a maximum threshold of 40 μm and/or temperatures colder than −38 °C.

As mentioned above, secondary activation can occur either after coalescence or when w accelerates above the cloud base, which increases the cooling rate. This might increase S to the extent that it exceeds S_{max} near the cloud base, even before the coalescence process dominance when the condensational growth is still dominant. While the secondary activation of droplets after coalescence was presented and discussed in a previous paper (Efraim et al., 2022), this study serves as a complementary one and discusses the physical principle of secondary activation during the condensational growth phase. Both studies together present a whole method of detecting *SAZ* from satellite observations. The conditions during coalescence are typically aerosol-limited, whereas the conditions at the focus of this study are often updraft-limited - the added drop nucleation occurs due to updraft acceleration. The condensational growth zone contains small droplets, so the newly activated ones are much less likely to reverse the growth trend with height like in the post-coalescence *SAZ*, but rather slow it to below adiabatic.

Hereafter, the microphysical zone in the cloud where secondary activation during the condensational growth occurs is referred to as SAZ_{cond}, and the secondary activation of droplets above the coalescence phase is referred to as SAZ_{coal}.

1.3. Secondary activation during the condensational growth phase, SAZ_{cond}

Additional condensation of water vapor above the level of S_{max} leads to a growth of the existing cloud droplets, i.e., condensational growth. This process further increases the integrated droplet surface area, decreases S, and usually prevents the activation of additional cloud droplets above that level (Rosenfeld, 2018). The LWC_a is divided over the single droplet mass of the existing cloud droplets ($M_{droplet}$), causing the N_d to remain relatively constant with height (Rogers and Yau, 1996; Freud et al., 2011; Rosenfeld et al., 2016). This is valid as long as the cloud is adiabatic and there is no droplet evaporation or activation of new CCN particles (Rosenfeld, 2018). Therefore, a linear relationship of LWC_a-$M_{droplet}$ ratio would denote an adiabatic part of the cloud. The adiabatic condensational growth phase is then determined by the most consecutive linear points of the LWC_a-$M_{droplet}$ ratio. This linear part should also be close to the cloud base and pass through the origin because when LWC_a is zero, there are no droplets. Fig. 1 illustrates the LWC_a [g/kg] as a function of $M_{droplet}$ [μg] for each temperature bin. The LWC_a is calculated based on the retrieved cloud base pressure and temperature and increases up to the cloud top (Freud et al., 2011). Assuming the droplets are spherical, the $M_{droplet}$ is calculated by the product of the droplet volume and the water density. As long as the LWC_a-$M_{droplet}$ ratio remains linear, the adiabaticity is preserved. This means that the LWC_a is divided equally between the existing cloud base N_d without losing or gaining droplets. If this ratio is no longer linear, it can either mean (1) droplet coalescence, where $M_{droplet}$ increases

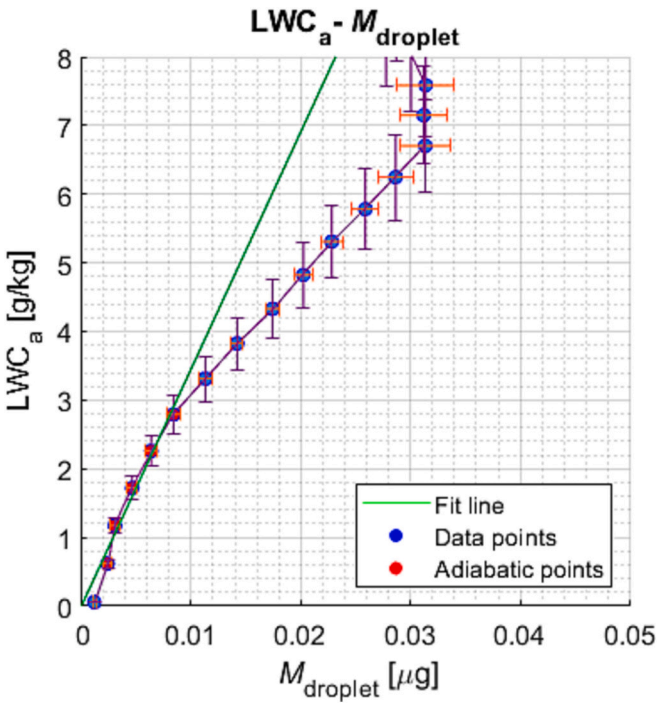

Fig. 1. Illustration of the adiabatic LWC (LWC_a [g/kg]; uncertainty: 15%) over droplet mass ($M_{droplet}$ [μg] uncertainty: 8%). The data was derived from a sample satellite-retrieved case study over the Amazon (−2.56°, −59.46°) from February 26th, 2018. Each point represents the calculated LWC_a and $M_{droplet}$ for each temperature bin. The LWC_a is calculated based on the cloud base pressure and temperature, and the $M_{droplet}$ is based on the mean-volume radius (r_v), where $r_v = \frac{r_e}{1.08}$ in the adiabatic part. The red points and the green fit line mark the part where the LWC_a-$M_{droplet}$ ratio is most linear and passes through (0,0). These are the adiabatic points by which the N_d at the cloud base is calculated. Any deviation or noise in the defined adiabatic points may cause a bias in retrieving the cloud base N_d. (For interpretation of the references to color in this figure legend, the reader is referred to the web version of this article.)

beyond adiabaticity; (2) precipitation, where $M_{droplet}$ decreases due to the removal of raindrops and remaining tiny drops; or (3) activation of new cloud droplets (i.e., SAZ_{cond}), which also decreases $M_{droplet}$.

As mentioned above, N_d is calculated based on the linear LWC_a-$M_{droplet}$ ratio. Any deviation from adiabaticity due to SAZ_{cond} in the defined linear part may cause an overestimation in the retrieval of cloud base N_d. This will be further discussed in Section 4. Another impact of SAZ_{cond} is the suppression of warm rain and possible cloud invigoration. Several studies suggested, based on aircraft and satellite measurements, that warm rain formation requires a cloud with r_e larger than 13–14 μm (Rosenfeld and Gutman, 1994; Gerber, 1996; Pinsky and Khain, 2002; VanZanten et al., 2005; Chen et al., 2008; Prabha et al., 2011; Konwar et al., 2012; Freud and Rosenfeld, 2012). The activation of tiny cloud droplets during the condensational growth inhibits the collision and coalescence processes and delays the droplets' growth into raindrops. This will be described by the model and with aircraft validations in Section 3.1 and Section 4, respectively.

This study describes and demonstrates the physical principle of secondary activation of droplets during the condensational growth of convective clouds. For this purpose, a spectral bin microphysics adiabatic parcel model was used to simulate the vertical profiles of several cloud properties for different aerosol size distribution (ASD) and w profiles. In addition, a method to detect SAZ_{cond} from a satellite is presented, and the impact of SAZ_{cond} on the satellite retrieval of N_d is discussed. The simulated cloud properties are described in Section 3.1. Case studies with and without a detectable SAZ_{cond} on satellite retrieved T-r_e and a discussion on the effect on the retrieved N_d are described in Section 3.2 and Section 4, respectively.

2. Methods

The methodology in this study is similar to the methodology presented in Efraim et al. (2022), therefore we describe it here concisely with the relevant adjustments for the SAZ_{cond} study.

2.1. Model description

The model used here is the Pinsky and Khain (2002) spectral bin adiabatic parcel model with 2000 bins, which describes the cloud microphysical properties of convective clouds in the water phase only (temperatures warmer than −10 °C). The initial thermodynamic conditions for the simulations, including pressure, temperature, relative humidity, and height, were measured below cloud bases during flight AC07 of the ACRIDICON-CHUVA campaign (Wendisch et al., 2016). The simulations are based on modified ASD measured below cloud bases in subsaturated conditions (Braga et al., 2021; Pöhlker et al., 2021), and on aerosol supply through the cloud base. This means that entrainment is not included according to the inhomogeneous mixing assumption. However, the results in such cases are expected to be similar: a reduction of r_e (e.g., Burnet and Brenguier, 2007; Andrejczuk et al., 2009; Devenish et al., 2012; Kumar et al., 2012; Pinsky et al., 2016). The simulated cloud properties are r_e, N_d, the total particle number concentration (N_a), S, rainwater fraction (RWF), and prescribed updraft (w) as a function of decreasing T to match the retrieval from the satellite. The temperature (°C) is correlated with the height (m) above the cloud via the moist adiabatic lapse rate (~ 6 °C/km). In the original use of the model (Pinsky and Khain, 2002) the w profiles are calculated by the sum of the buoyancy and friction forces, according to an input sounding profile. In this study, the w profiles are prescribed to control the rate of increase of the production term of S. The w profiles represent typical values taken from measurements (Anderson et al., 2005; Giangrande et al., 2016; Braga et al., 2017; Marinescu et al., 2020).

The RWF is defined as the ratio between the rainwater content (drops with a diameter > 50 μm) and the total water content. It increases as coalescence starts and decreases as the raindrops precipitate from the cloud. If there is no new droplet activation, RWF increases with decreasing T up to unity when the smallest drops grow beyond the threshold of 50 μm in diameter. In the case of SAZ occurrence, the RWF decreases as the new small droplets delay the conversion into raindrops. Although we focus here on the condensational growth phase, the RWF is present as it is affected by the SAZ_{cond}. Generally, clouds that completely rain out cannot develop beyond that point due to a lack of condensation and buoyancy. However, in this study, the model forces the cloud to grow beyond the point of total rainout to illustrate how secondary activation changes the T-r_e profile compared to the alternative that is rarely realized in nature. The T-r_e profile for each simulation (e.g., Fig. 2D and 3D) shows the adiabatic r_e curves under the assumption of condensational growth only for each cloud base N_d (grey lines). The adiabatic curves are calculated based on the LWC_a and the corresponding development of r_e based on the cloud base temperature and pressure (Rosenfeld et al., 2016). The deviations between the actual and the adiabatic T-r_e profiles define the dominant microphysical zones (Efraim et al., 2022).

To emphasize the impact of different ASD and w profiles on the microstructure of the cloud and the SAZ, several sets of simulations were performed. The first two simulations (Fig. 2 and Fig. 3) present the impact of SAZ in general on the cloud properties, and the other ones (Fig. 4 and Fig. 5) focus on the temperature of SAZ_{cond} initiation. The first simulation (Fig. 2) uses a fixed ASD and three prescribed w profiles and the second one (Fig. 3) uses two ASD and a fixed w profile.

This thorough model describes the fundamental physical processes by simplifying environmental factors. However, it is well suited to illustrate the physical principle of SAZ_{cond} and the expected behavior of such a process on the cloud properties.

2.2. Satellite T-r_e retrieval

The satellite retrieval case studies in Section 3.2 were obtained from the Visible Infrared Imaging Radiometer Suite (VIIRS) passive sensor onboard the Suomi National Polar-orbiting Partnership (S-NPP) satellite. This sensor has sufficient resolution to accurately resolve the vertical structure of convective clouds by retrieving its T-r_e profile. The wavelengths used to retrieve the T-r_e profile are 10.8 μm and 3.7 μm for T and r_e, respectively (Rosenfeld et al., 2014b). The uncertainty values of the satellite-retrieved properties are T (0.2 °C), r_e (8%), and LWC_a (15%) (Rosenfeld et al., 2016). The satellite retrieval method assumes ergodicity, meaning that a snapshot of the T-r_e profile of a cloud cluster gives the same information as obtained by tracking a single convective system throughout its vertical evolution (Arakawa and Schubert, 1974; Lensky and Rosenfeld, 2006). In addition, assuming no precipitation is falling, the cloud top pixel is considered to have the same r_e value as more developed clouds at the same height (Freud et al., 2008; Rosenfeld and Lensky, 1998).

Using a designated IDL software, cloud scenes of interest were manually sampled on the satellite image to minimize obstruction by multilayer or semi-transparent clouds. Then, a cloud mask algorithm (Zhu et al., 2014) filters out the partially filled cloudy pixels to reduce associated errors. The distortion caused by the satellite and the solar zenith angle is reduced by taking cloud scenes between 30° and − 20°, and below 65°, respectively. The 30th percentile for all r_e values within each bin is calculated, resulting in a continuous T-r_e profile that captures the clouds in their growing phase, where the effect of aerosols is mostly reflected (Lensky and Rosenfeld, 2006; Rosenfeld et al., 2008; Rosenfeld et al., 2016). T-r_e profiles obtained in different locations yield similar findings for similar environments (e.g., Lensky and Rosenfeld, 2006; Rosenfeld, 2007; Rosenfeld et al., 2008; Huang et al., 2022) implying robust, credible, and applicable worldwide method. An objective algorithm analyzes the retrieved T-r_e profiles and divides the cloud into different microphysical zones (Efraim et al., 2022), where the condensational growth microphysical zone is the focus of this study.

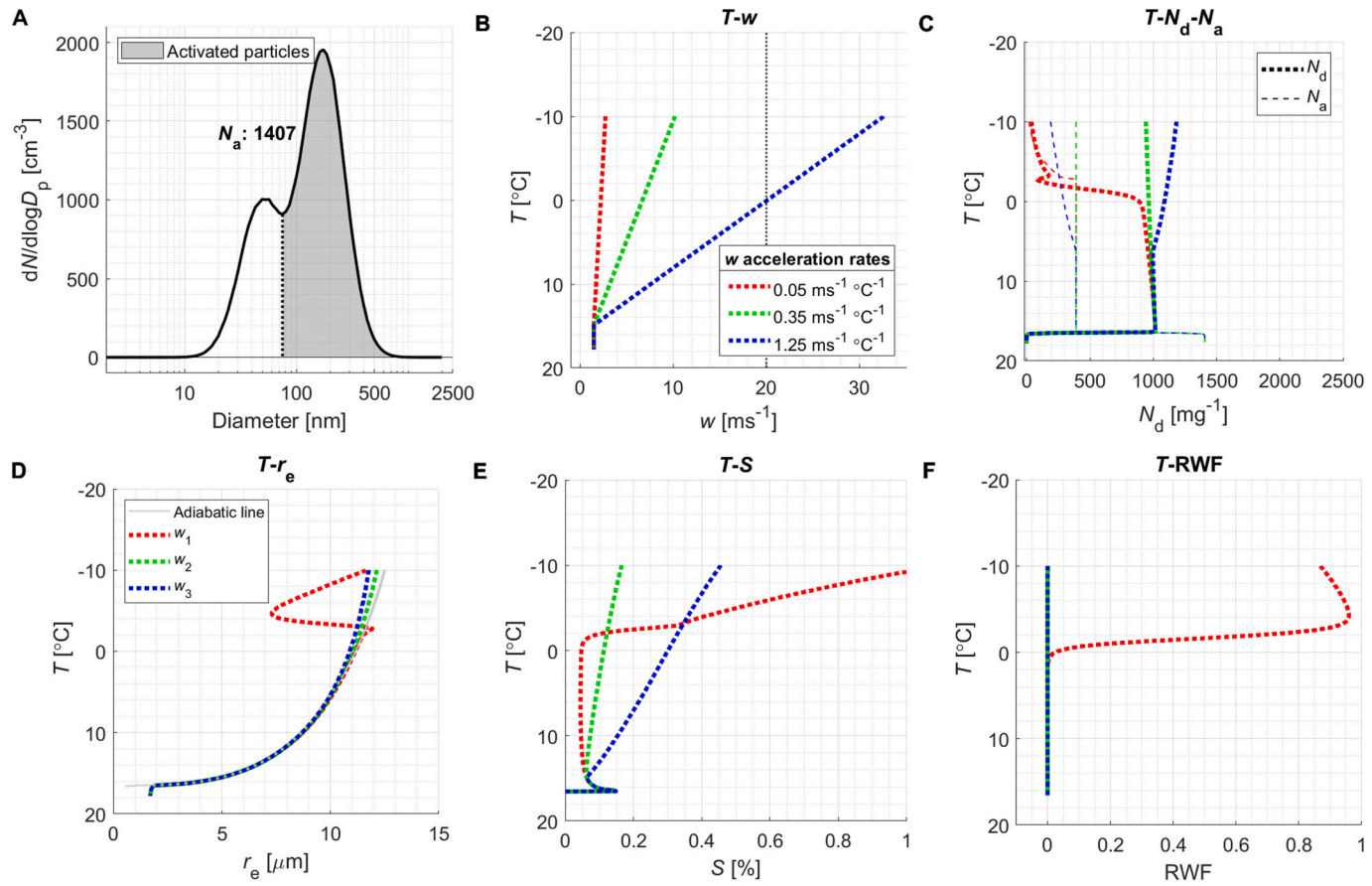

Fig. 2. Simulations of cloud properties for a fixed aerosol size distribution (ASD) and three prescribed updraft profiles (w). Panel A shows the bimodal ASD with a high concentration of accumulation mode particles and a lower concentration of Aitken mode particles. The total particle number concentration (N_a) below the cloud base is 1407 cm^{-3}. The shaded grey marks the calculated activated particles at the cloud base. Panel B shows the prescribed w profiles with a constant w speed of 1.5 ms^{-1} up to the cloud base and then different acceleration rates, where w_1 (red dashed line) has the lowest acceleration rate (0.05 ms^{-1} °C^{-1}) and is close to constant w with height; w_2 (green dashed line) has a higher acceleration rate (0.35 ms^{-1} °C^{-1}); and w_3 (blue dashed line) has the strongest acceleration rate (1.25 ms^{-1} °C^{-1}). Panels C—F show the different cloud properties, where the color of the lines is related to the same-colored w profile in each panel. Panel C shows the number concentration of cloud droplets (N_d) and N_a profile in units of mg^{-1} to avoid the consideration of the change of air density with height; Panel D shows the effective radius (r_e) profile, where the grey line is the adiabatic curve, calculated based on the cloud base pressure and temperature; Panel E shows the vertical profile of supersaturation over water (S) and Panel F shows the vertical rainwater fraction (RWF) profile. (For interpretation of the references to color in this figure legend, the reader is referred to the web version of this article.)

2.3. Aerosol observations at the Amazon Tall Tower Observatory

For each of the case studies described in Section 3.2, an ASD was measured at the Amazon Tall Tower Observatory (ATTO). This site is located in the Amazon Basin (2.145°S, 59.004°W at 130 m above sea level) and uses a Scanning Mobility Particle Sizer (SMPS) at 60 m height above the surface (Franco et al., 2022). In addition, this site monitors fundamental climatic and atmospheric parameters such as temperature, pressure, wind profiles, advection of air mass, relative humidity, and precipitation (Andreae et al., 2015). These parameters were used to determine the coupling state of the chosen cloud scene case studies, where the air sampled at ATTO fed the sampled clouds.

3. Results

3.1. Simulations of SAZ_{cond}

This section presents the convective cloud simulations and the effect of different inputs of ASD and w profiles on the microphysical zones focusing on the existence and properties of SAZ_{cond}. The panels in each figure of the cloud properties simulations (Fig. 2 and Fig. 3) include the ASD in panel A; The w profiles in panel B; the N_d and N_a profiles in panel C; the r_e profile in panel D; the S profile in panel E; and the RWF profile in panel F.

3.1.1. Fixed ASD

The input of the first simulation includes (1) a representative bimodal ASD with a high concentration of accumulation mode particles that serve as CCN at a supersaturation of approximately 0.2% and a smaller Aitken mode particle population (e.g., Pöhlker et al., 2016, 2018; Franco et al., 2022). The total N_a is 1407 cm^{-3} (Fig. 2A); (2) Three prescribed w profiles (Fig. 2B) with a typical initial speed of 1.5 ms^{-1} at cloud base (Braga et al., 2017) and then different acceleration rates with height. The first w profile (w_1, red dashed line) has an acceleration rate of 0.05 ms^{-1} °C^{-1}. It has the lowest slope and the closest one to constant w. w_2 (green dashed line) has a higher acceleration rate of 0.35 ms^{-1} °C^{-1}, and w_3 has the highest acceleration rate of 1.25 ms^{-1} °C^{-1} (blue dashed line). According to the T-N_d-N_a profile (Fig. 2C), the cloud's primary activation, consisting of the accumulation mode only (Fig. 2A), is the same for all three w profiles due to the same value at the cloud base. Under specific conditions, the remaining Aitken mode particles have the potential for later activation. After the primary activation, N_d stays nearly constant with decreasing T and only decreases slightly due to the minor coalescence process above the cloud base. This is consistent with the constant N_a concentration with decreasing T, meaning that no new activation of droplets occurs. The T-r_e profile (Fig. 2D) shows that,

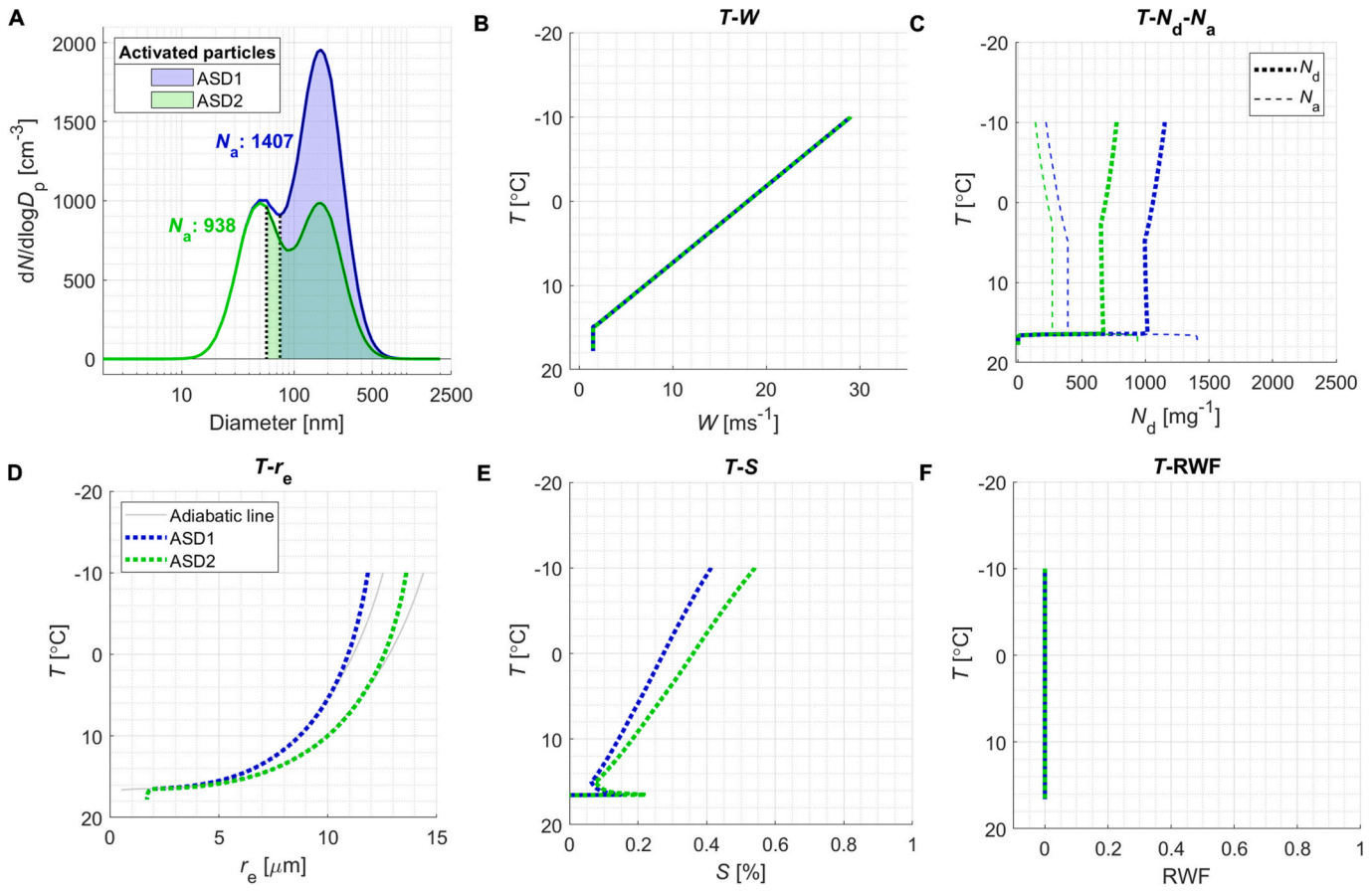

Fig. 3. Simulations of cloud properties for fixed prescribed updraft (w) profile (panel B) and two different aerosol size distributions (ASD) (panel A). The w profile is the same as w_3 in Fig. 2, with a constant w of 1.5 ms^{-1} up to the cloud base and then an acceleration rate of 1.25 ms^{-1} °C^{-1}. The first ASD (ASD1, blue) is the same as illustrated in Fig. 2, with the same N_a of 1407 cm^{-3}. The second ASD (ASD2, green) has the same Aitken mode as the blue one but has a lower accumulation mode. The N_a of ASD2 is 938 cm^{-3}. Panels C—F show the different cloud properties as described in Fig. 2, except the color of the lines in this figure is related to the same-colored ASD in each panel. (For interpretation of the references to color in this figure legend, the reader is referred to the web version of this article.)

at first, r_e increases at the same rate as the adiabatic curve for the same cloud base N_d. This means that during this phase, the dominant microphysical process is condensational growth. For the w_1 case (red dashed line in Fig. 2D), the coalescence and collision processes start to dominate at ~0 °C and lead to rainout at that level, as shown in the T-RWF profile (Fig. 2F). The N_d starts to decrease sharply at the level of rain initiation, as the coalescence merges many cloud droplets into fewer raindrops. The coalescence and rainout reduce the integrated droplet surface area available for condensation, leading to S exceeding S_{max}. As a result, smaller particles with lower critical S (S_c) are activated as cloud droplets. This is the SAZ_{coal} as defined and shown in Efraim et al. (2022). The SAZ_{coal} is easily seen on the T-N_d-N_a profile as the increase of N_d and reduction of N_a at ~ − 3 °C. It is also noticeable in the T-r_e profile, as the r_e growth rate exceeds the adiabatic curve when the coalescence becomes dominant and turns negative with the activation of new droplets in the environment of coalesced ones. In nature, this could also happen due to the entrainment of particles with low S_c from the lateral boundaries of the cloud (Warner, 1973; Latham and Reed, 1977; Baker et al., 1980). For the w_2 case, r_e remains adiabatic up to cloud top, and rain initiation is delayed altogether (green line in Fig. 2F). When w accelerates even faster (w_3; blue line in Fig. 2C), the strong cooling rate causes a high enough S to exceed S_{max} and to activate new droplets even during the condensational growth, representing SAZ_{cond}. In this case, N_d starts to increase during the dominant condensational growth phase at ~6 °C. In the environment of the small droplets with little coalescence, the newly activated ones slow down the r_e growth rate and it becomes less than adiabatic (blue dashed line in Fig. 2D). The activation of new droplets during the condensational growth delays the coalescence process and the initiation of the rain. As seen in the T-RWF profile, no rain is initiated until cloud top (blue dashed line in Fig. 2F).

Eventually, for the same ASD, the highest w acceleration causes SAZ_{cond} while the lower ones may keep the r_e adiabatic or cause SAZ_{coal}.

3.1.2. *Fixed w profile*

The input of the second simulation includes: (1) two bimodal ASD, where ASD1 is identical to the ASD in the previous simulation (blue line in Fig. 3A), whereas ASD2 has the same concentration of Aitken particles, but a lower concentration of accumulation mode particles (green line in Fig. 3A). The N_a is 1407 cm^{-3} for ASD1 and 938 cm^{-3} for ASD2; (2) One prescribed w profile (Fig. 3B) identical to the w_3 profile from the first simulation. The T-N_d-N_a profile (Fig. 3C) shows a higher concentration of activated N_d at the cloud base for the ASD1 case (blue dashed line), which has a higher concentration of accumulation mode particles. Therefore, S_{max} of the ASD1 case (blue dashed line in Fig. 3E) is smaller than the one of the ASD2 case (green dashed line). However, the cloud base N_d is smaller than the N_a for both cases, meaning that there are unactivated interstitial particles within the cloud parcel. After the primary activation, N_d stays relatively constant with height, and the r_e increases at the same rate as the idealized adiabatic curves for each cloud base N_d (Fig. 3D), indicating that condensational growth is the dominant microphysical process. For the prescribed w profile in this simulation, SAZ_{cond} appears for both cases, although, the temperature of SAZ_{cond} initiation changes. With the constant increase of w and cooling rate, S exceeds the initially smaller S_{max} for the ASD1 case at a warmer

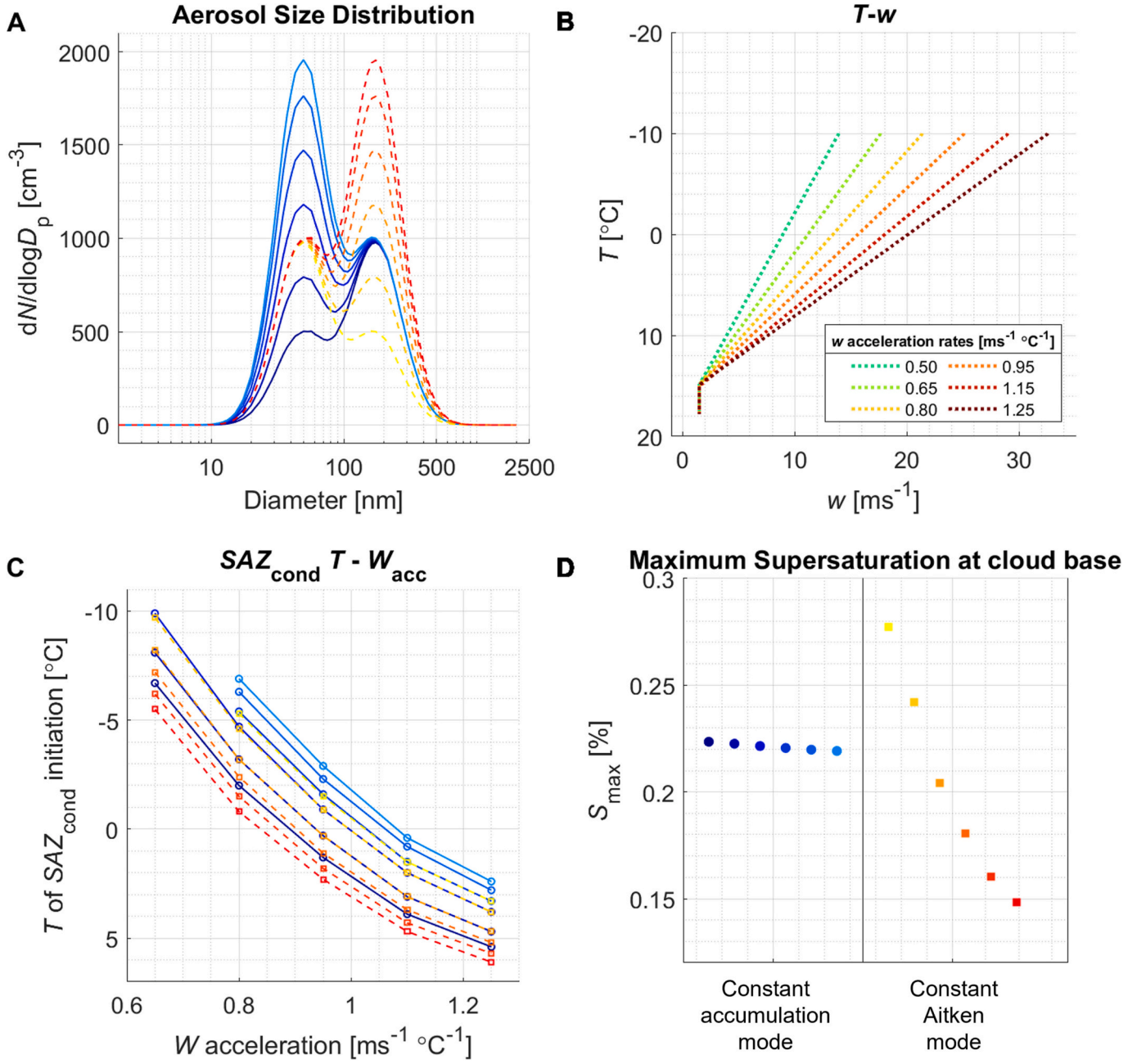

Fig. 4. The temperature of SAZ_{cond} initiation for various aerosol size distributions (ASD) and updraft (w) profiles. Panel A shows the different ASD, where the warm color scaled lines (red to yellow) are ASD with constant Aitken mode and various accumulation modes; and the cold color scaled lines (dark to light blue) are ASD with constant accumulation mode and various Aitken modes. Panel B shows the different w profiles, where they all have w_b of 1.5 ms^{-1} and different acceleration rates. Panel C shows the temperature of SAZ_{cond} initiation as a function of the w acceleration rate and Panel D shows the maximum supersaturation at cloud base (S_{max}), where in both panels each colored point or line is related to the same-colored ASD color in panel A. (For interpretation of the references to color in this figure legend, the reader is referred to the web version of this article.)

temperature, causing SAZ_{cond} to occur at a lower altitude. The S_c increases as the interstitial particles' size and the air temperature decrease. Thus, a higher S_c must be reached to activate further interstitial particles in the ASD2 case. Therefore, the SAZ_{cond} occurs slightly higher than the point where S exceeds S_{max}. The r_e growth rate in both cases becomes less than adiabatic, but for the lower-level SAZ_{cond}, it occurs at warmer T (or lower altitude). The secondary activation of a higher concentration of particles in the ASD1 case (blue dashed line in Fig. 3D) results in the r_e growth rate decrease to smaller values than for the ASD2 case (green dashed line). The activation of new droplets delays the coalescence process and the initiation of the rain in both cases up to the cloud top (Fig. 3F).

Eventually, for the same strong w, a case with a more prominent accumulation mode will experience SAZ_{cond} in warmer temperatures and lead to smaller r_e because of more available particles for activation with lower S_c in the rising parcel. The cloud microstructure profiles for the simulations of the w_1 and w_2 profiles with ASD2 are shown in the supplements (Fig. S1).

Fig. 4 summarizes the effect of various ASD and w profiles on the temperature of SAZ_{cond} initiation. The input for this set of model runs includes (1) twelve ASD with various accumulation and Aitken mode sizes (Fig. 4A); and (2) six w profiles with a constant w_b of 1.5 ms^{-1} and different accelerations (Fig. 4B). As shown in the figure, generally, weaker w acceleration results in a colder temperature of SAZ_{cond}

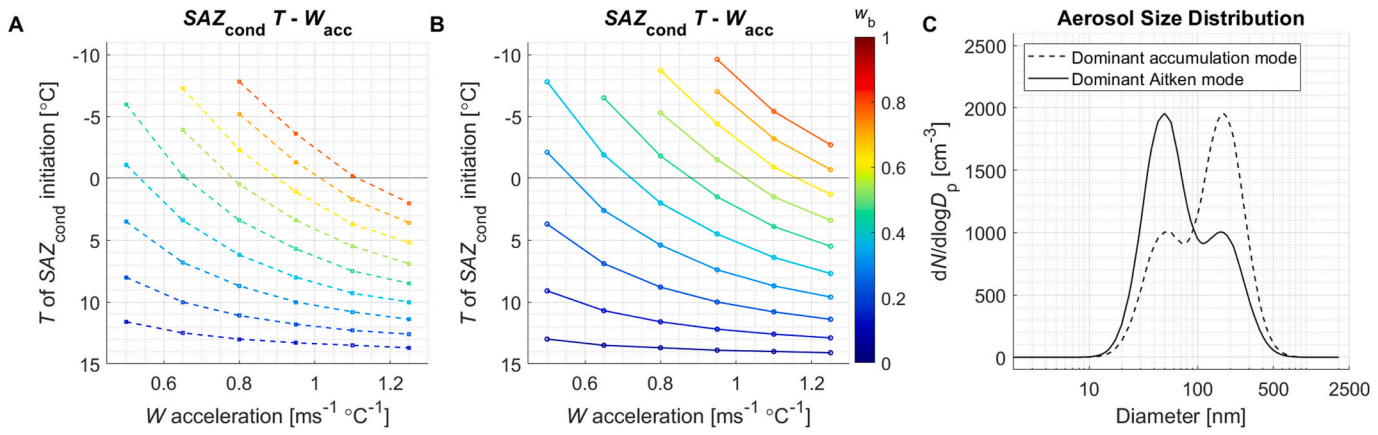

Fig. 5. The temperature of SAZ_{cond} initiation for two different aerosol size distributions (ASD), updraft (w) profiles, and cloud base w (w_b). Panel A shows the two ASD with dominant accumulation (dashed) or Aitken (solid) mode. Panels B and C show the temperature of SAZ_{cond} initiation as a function of the w acceleration and the w_b for each ASD. The w profiles are described in panel B of Fig. 4.

initiation, because S exceeds the cloud base S_{max} higher in the cloud, due to lower cooling rate.

The dashed warm colored lines (yellow to red color scale) represent ASD where the Aitken mode is constant (peak at $dN/dlogD_p = 1000$ cm^{-3}) and the accumulation mode varies from peak at $dN/dlogD_p = 500$ cm^{-3} to $dN/dlogD_p = 2000$ cm^{-3}. In the extreme case of very high accumulation mode (darkest red), S_{max} is lowest (0.14%) (Fig. 4D) due to the activation of many of the largest particles. The needed w acceleration for S_{max} exceedance is lower compared to ASD with lower accumulation mode, where S_{max} is higher due to the activation of fewer particles (Fig. 4D). Therefore, the temperature of SAZ_{cond} initiation is warmer. In addition, increasing the accumulation mode means more available particles with sufficient S_c for activation in the S values beyond S_{max}. On the other hand, the cold colored lines (dark to light blue color scale) represent ASD where the accumulation mode is constant (peak at $dN/dlogD_p = 1000$ cm^{-3}) and the Aitken mode varies from peak at $dN/dlogD_p = 500$ cm^{-3} to $dN/dlogD_p = 2000$ cm^{-3}. In these cases, S_{max} does not change as much compared to the constant Aitken mode cases (Fig. 4D). This is due to the activation of the whole accumulation mode at the cloud base. When the Aitken mode is higher (lighter blue), more particles are added to the accumulation mode and are activated at the cloud base, thus S_{max} slightly decreases. In cases with lower Aitken mode (darker blue), the temperature of SAZ_{cond} initiation is warmer for the same w acceleration, because there are more available particles with sufficient S_c for activation (fewer smaller ones). This occurs even though S_{max} is slightly higher in darker blue cases because there are fewer activated particles to lower the supersaturation.

In addition, there are ASD in intermediate states with either low accumulation and/or low Aitken modes, where the temperature of SAZ_{cond} initiation is a matter of how many particles are activated at the cloud base against how many activate due to the w acceleration rate.

Another factor that determines the temperature of SAZ_{cond} initiation is the cloud base w (w_b). Fig. 5 shows the temperature of SAZ_{cond} initiation as a function of the w acceleration for different w_b (panels A and B). The model was run for two ASD with constant accumulation mode and high Aitken mode (solid line in Fig. 5C), and vice versa (dashed line in Fig. 5C). According to this figure, for both ASD, smaller w_b leads to warmer temperature of SAZ_{cond} initiation. The w_b determines the N_d at the cloud base, thus smaller values activate lower N_d, resulting in more available particles for activation during the condensational growth phase due to the prescribed w acceleration.

3.2. Detection of SAZ_{cond} based on satellite-retrieved T-re profiles

The different microphysical zones in convective clouds and the method for their detection by the T-r_e profile analysis have been fully described in Efraim et al. (2022) and also briefly in Section 1.2. However, the newly defined SAZ_{cond} is less readily detected since it is a part of the defined condensational growth phase. Still, it can be identified by analyzing the small fluctuations within the condensational growth points. These small fluctuations can be either noise, due to retrieval uncertainty (Freud et al., 2011; Rosenfeld et al., 2016), in which case these points should still be defined as condensational growth; or SAZ_{cond} signal, representing the appearance of smaller droplets within the condensational growth phase.

To analyze the fluctuations in the condensational growth points, we used the profile of the natural logarithm of the adiabatic N_d with decreasing T (T-ln(N_{da})). The value of ln(N_{da}) is calculated by taking the natural logarithm of the LWC_a-$M_{droplet}$ ratio for each temperature bin, for the adiabatic points. Using the ln(N_{da}), instead of N_{da}, emphasizes the relative change in N_{da} rather than the absolute change. The ln(N_{da}) was linearly segmented by the trend of the points. Ideally, the ln(N_{da}) should be quite constant during the condensational growth and any increase can be either due to noise or a signal. The SAZ_{cond} is identified where a significant increase of ln(N_{da}) occurs.

This section presents two convective cloud scenes as case studies with and without a detected SAZ_{cond} and an application of a method to detect the SAZ_{cond} by remote sensing. Both cloud scenes were sampled over the ATTO region, where the ASD of the air feeding the clouds was measured. Even though both cases include coalescence or ice formation, we focus on the adiabatic non-precipitating part only. Each case study (Fig. 6 and Fig. 7) presents the satellite overpass image in panel A, the 1-h average ASD of the feeding air before the satellite overpass in panel B, the LWC_a-$M_{droplet}$ ratio in panel C, the T-r_e profile in panel D and E, and the T-ln(N_{da}) profile in panel F.

Cloud scene A is an example of a case without SAZ_{cond}. The cloud scene is marked by a red polygon on a Day Natural color scheme satellite image (Lensky and Rosenfeld, 2008). In this case, a cluster of cumulus congestus clouds was taken within ~25 km of the ATTO site. The satellite overpass was on the 6th of July 2017 at 17:40 UTC. The adiabatic points are marked in red on the LWC_a-$M_{droplet}$ profile (Fig. 6C). These points have the best linear fit with the origin ($R^2 = 0.995$), thus they define the condensational growth phase. The N_d at the cloud base is then determined by the linear ratio of LWC_a-$M_{droplet}$. The grey line on the T-r_e profile (Fig. 6D and E) is the adiabatic curve calculated by the cloud base temperature and pressure for the specific retrieved N_d. The defined condensational growth points (red points) agree with the adiabatic curve until the coalescence begins and exceeds adiabaticity (Fig. 6D and E). The adiabatic T-ln(N_{da}) profile (Fig. 6F) shows a slight increase of 0.079 in the ln(N_{da}) for the adiabatic points. To determine whether it is noise or signal we examine the ASD. The calculated N_d based on the linear LWC_a-$M_{droplet}$ ratio is 836 cm^{-3}. The 1-h average ASD (Fig. 6B)

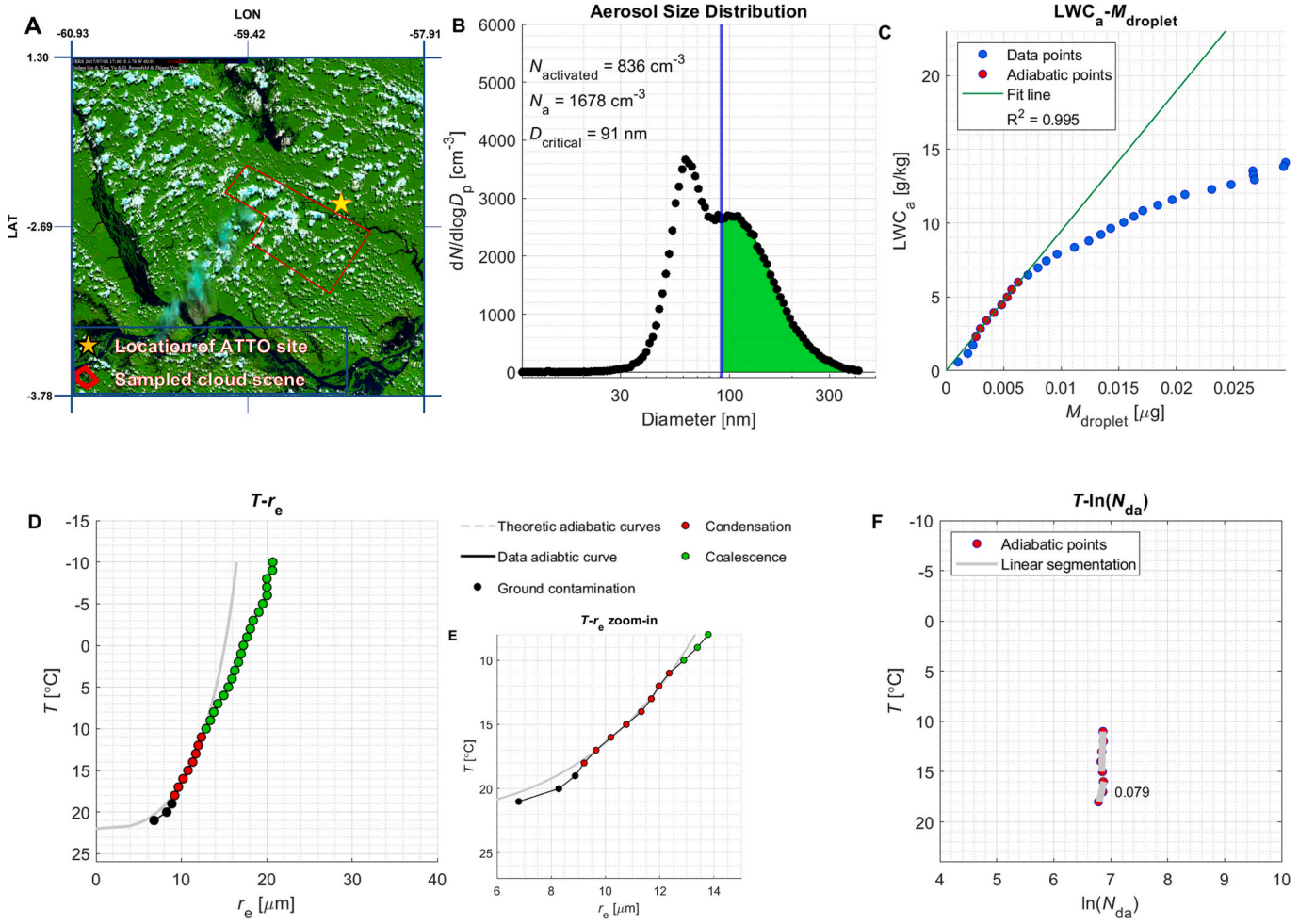

Fig. 6. Satellite-retrieved cloud microphysical profiles in the ATTO region without indications for secondary droplet activation during the condensational growth phase (SAZ_{cond}). Panel A shows the Day Natural color scheme satellite image with the ATTO site marked as the star and the sampled cloud scene shown as a red polygon (Cloud scene A). Panel B shows the 1-h average ASD at ATTO before the satellite overpass, with the particle fraction activated as cloud droplets being shown as green shading under the curve. Panel C shows the LWC$_a$-$M_{droplet}$ ratio where the red points are defined as the adiabatic ones, with the best fit with the origin (R^2 = 0.995). The adiabatic points are marked as the condensational growth points on the T-r_e profile (red points in Panel D). The grey line in the same panel is the calculated adiabatic curve for the specific retrieved N_d. Panel E shows an enhanced T-r_e profile focused on the adiabatic part. The T-ln(N_{da}) profile (Panel F) shows only the adiabatic points (red points in Panel D) and the trend lines with decreasing T. The value in Panel F (0.079) is the slope of the positive trend line. (For interpretation of the references to color in this figure legend, the reader is referred to the web version of this article.)

has a well-defined Hoppel minimum at 85 nm. The Hoppel minimum is a size separation gap between two size modes, which usually indicates the size of the smallest particles that can serve as CCN for the given thermodynamic conditions due to cloud processing (Hoppel and Frick, 1986; Hudson et al., 2015). Summing the N_d largest particles on the ASD in Fig. 6B (green shading) yields the smallest diameter to be activated, i.e., the critical diameter, since the larger particles are activated first. In this case, the critical diameter is 91 nm. This suggests that the activated particles at the cloud base are accumulation mode particles down to that threshold. The good agreement of the retrieved N_d with the concentration of the accumulation mode particles implies that the fluctuations in the condensational points are likely to be noise and the case is without SAZ_{cond}. That is because no significant overestimation of N_d was found, as opposed to the next presented Cloud scene B.

As opposed to the previous case study, Cloud scene B (red polygon in Fig. 7A) is an example of a case with a possible SAZ_{cond}. The sampled cloud is a developed cumulonimbus ~70 km from ATTO. The satellite overpass was on the 1st of July 2017 at 17:30 UTC. The 1-h average ASD for Cloud scene B (Fig. 7B) has a well-defined Hoppel minimum at 91 nm and N_a of 932 cm^{-3}. The LWC$_a$-$M_{droplet}$ ratio profile (Fig. 7C) defined the adiabatic points (red points) with a linear fit of $R^2 = 0.916$. These points are also in good agreement with the adiabatic curve on the T-r_e profile (Fig. 7D and E). However, the adiabatic T-ln(N_{da}) (Fig. 7F) shows a larger increase in ln(N_{da}) of 0.32, compared to Cloud scene A (0.079). This suggests larger fluctuations in the adiabatic points. The calculated N_d based on the linear LWC$_a$-$M_{droplet}$ ratio is 1211 cm^{-3}, actually exceeding the accumulation mode particles that usually relate to primary activation, let alone the total N_a measured at ATTO. Even with allowing for possible differences in aerosol concentrations between ATTO and the location of the cloud as well as a potential overestimation of the retrieved N_d, this would imply that more particles were activated than the supplied ones. Therefore, the fluctuations in the adiabatic points, in this case, are implied to be a signal of potential activation of extra cloud droplets during the condensational growth which leads to a bias in the calculated adiabatic N_d. Presumably, if there was no SAZ_{cond} steepening the adiabatic line, it would be less vertical, resulting in a lower N_d. The tendency of the line towards a higher slope, due to the appearance of small droplets in the overall condensational growth phase, as well as the result biased N_d, indicates the likelihood of a potential SAZ_{cond}. This is distinct from noise or retrieval bias, which would shift the entire profile while maintaining the same slope. This will be further discussed in the next section.

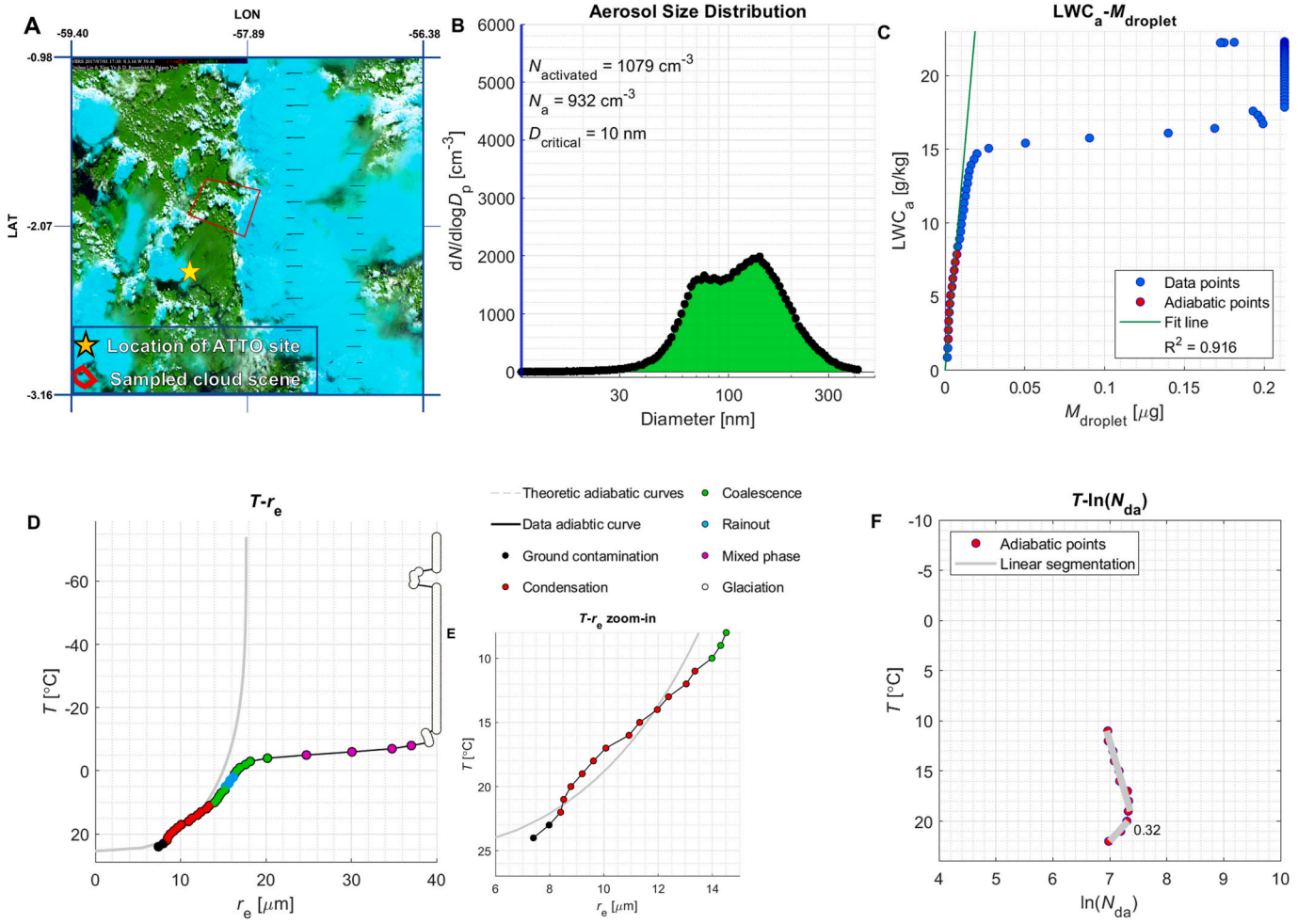

Fig. 7. Satellite-retrieved cloud microphysical profiles in the ATTO region with indications for secondary droplet activation during the condensational growth phase (SAZ_{cond}). Panels A-F have similar descriptions as in Fig. 6. However, the adiabatic points in panel C have R^2 of 0.916 and the value of the slope of the positive trend line in panel F is 0.32.

4. Discussion

The *SAZ* during condensational growth (SAZ_{cond}) may be detectable in the *T*-r_e profile as a slowdown of the r_e growth rate to less than the adiabatic one during the condensational growth phase, as shown in Cloud scene B in the previous section. It was also described by the model, in Section 3.1, where the r_e growth rate was reduced below the adiabatic values in cases of droplet activation during condensational growth (blue line in Fig. 2D and blue and green lines in Fig. 3D). This can occur due to an increase in *w* or at the same *w*, for different ASD. In nature, the SAZ_{cond} can occur also due to the entrainment of particles with low S_c, which can be activated at the existing *S* during the dominant condensational growth. However, both mechanisms result in the reduction of r_e. As seen in Cloud scene B, SAZ_{cond} may cause an overestimation of the satellite-retrieved N_d.

As mentioned in Sections 1.1 and 1.3, the adiabatic cloud base N_d can be approximated by the ratio of adiabatic LWC (LWC_a) to the mass of a single droplet ($M_{droplet}$), where $M_{droplet}$ is calculated based on the mean-volume radius (r_v) where $r_v = \frac{r_e}{1.08}$ in an adiabatic process (Freud et al., 2011). Additional droplet activation reduces the drop size for the same LWC_a, thus drop growth rate becomes less than adiabatic. This results in a calculated N_d above the adiabatic N_d at the cloud base. Another way to look at it is by observing the slope of the LWC_a-$M_{droplet}$ ratio, which is essentially the adiabatic N_d. Adding small droplets in the adiabatic part due to SAZ_{cond} will lower the $M_{droplet}$ and increase the adiabatic N_d to above the original value at the cloud base. The explicit formulas for the calculation of r_e and r_v are:

$$r_e = \frac{\int N(r) r^3 dr}{\int N(r) r^2 dr} \quad (1)$$

$$r_v = \left(\frac{3 \bullet LWC}{4\pi \rho_w N}\right)^{\frac{1}{3}} \quad (2)$$

Where *N* and *r* are the droplet concentration and radii, respectively, and ρ_w is the density of water (Freud and Rosenfeld, 2012). Adding *N* droplets with a small *r* above the cloud base due to SAZ_{cond} would not reduce the r_e as much as it would reduce r_v, assuming unchanged LWC_a. Therefore, the retrieved N_d under the assumption that all droplets were activated at the cloud base would give a larger N_d compared to the actual N_d at the cloud base and might even exceed the total CCN as shown in Cloud scene B. Another reason that might cause an overestimation of the retrieved N_d is the use of more adiabatic points with less certainty. Supposedly, taking only the first point on the adiabatic curve would suffice in the calculation of N_d, since it already gives the ratio of LWC_a to $M_{droplet}$. However, for the calculation of N_d, it is important to identify the whole adiabatic part of the *T*-r_e to avoid any biases due to surface contamination (Rosenfeld et al., 2016; Yue et al., 2019; Efraim et al., 2022). To reduce this uncertainty, the algorithm does not rely merely on the first point but rather includes more points above, as long as they are in good fit with the adiabatic curve. If these points include fluctuations due to SAZ_{cond}, the LWC_a-$M_{droplet}$ ratio would be larger, hence a larger N_d.

An additional impact of the SAZ_{cond}, as shown by the model, is the suppression of warm rain. This was also observed by in-situ measurements of T-r_e profiles from cloud probes in several flights during the ACRIDICON–CHUVA campaign (Wendisch et al., 2016), which showed that the measured N_d was larger above the cloud base than at the cloud base (Braga et al., 2017). During flights AC08, AC12, and AC20 strong w (up to 15 ms^{-1}) was measured above the cloud base. The strong w increased S and allowed for more CCN activation. The measured profiles of r_e were smaller than the estimated adiabatic r_e profile and its values were smaller than 13 μm, indicating the suppression of raindrop formation. Measured droplet size distribution from the cloud probe on the aircraft validated that indeed no raindrops were observed during these flights. Instead, ice particles were formed above the 0 °C isotherm (Braga et al., 2017) where the cloud could reach due to the suppression of the warm rain.

As described in Section 3.2, the minor fluctuation of the condensational growth can result from either noise (e.g., Cloud scene A) or an actual signal of SAZ_{cond} (e.g., Cloud scene B). However, it can be argued that the supposed SAZ_{cond} is merely due to deviation from adiabaticity because of mixing that changes the 1.08 ratio or a matter of satellite retrieval uncertainties, such as the r_e.

Regarding the deviation from the adiabaticity argument, we rely on the strong assumption of inhomogeneous mixing in convective clouds (references in Section 1.1), thus the cloud r_e is considered to be adiabatic. Moreover, we rely on representative atmospheric measurements from ATTO that show no abnormality in the relative humidity, precipitation, or air temperature near the satellite overpass time. This suggests that there is no evidence of the mixing of a different kind of air parcel into the cloud.

As for the uncertainty in the r_e retrieval, it can be attributed to three main factors: (1) 3D effects, (2) pixel inhomogeneity, (3) and distortion due to large backscatter angles. 3D effects, such as illuminating and shadowing, can lead to a significant r_e bias (Marshak and Davis, 2005; Davis and Marshak, 2010; Marshak et al., 2006; Zhang et al., 2012). However, the accuracy of retrieved r_e from MODIS (Moderate Resolution Imaging Spectroradiometer) satellite sensor was found to be the best at the 3.7 μm channel in non-precipitating clouds (King et al., 2013; Rosenfeld et al., 2016), because the 3D effects tend to have the lowest impact in this wavelength. This is due to the largest absorption and shortest mean free path of the photons (Zhang et al., 2012). Therefore, the use of this channel leads to minimal effect by cloud inhomogeneities and 3D effects (Rosenfeld et al., 2004; Zhang and Platnick, 2011; Grosvenor and Wood, 2014). The VIIRS detector used in this study, which has a much finer resolution than MODIS (Rosenfeld et al., 2014a, 2014b; Yue et al., 2019), further reduces the uncertainty related to the first two reasons mentioned above.

The distortion due to the backscattering angle is solved by applying the retrieval restrictions mentioned in Section 2.2. However, by using observations in the cloud scale, this bias would only cause a shift in the whole r_e profile. In this study, we focus mainly on the trend and not the absolute values of r_e, so even with shifting of the r_e profile the trend is preserved. Therefore, the importance of the r_e uncertainty in that manner is reduced, considering the similar satellite-retrieved and modeled r_e behavior at the scale of the same cloud.

Nevertheless, this uncertainty should not be neglected. Based on initial statistical analysis, a threshold value of approximately 0.2 for ln (Nda) was established to distinguish between noise and signal. However, this threshold should be strengthened by incorporating more observational data.

Here we simply outline the underlying physical principle and present a case study with a potential SAZ_{cond}. Further statistical results along with validations of measured ASD below the clouds necessitate additional research.

5. Conclusions

Aerosol particles can be activated into cloud droplets in convective clouds above the cloud base. The microphysical zone in the cloud where it occurs is referred to as the secondary activation zone (*SAZ*). The detection of *SAZ* based on T-r_e profiles allows the identification of a significant occurrence of new droplet activation above the cloud base, either after the dominant coalescence of droplets (SAZ_{coal}) or during the dominant condensational growth of the cloud droplets (SAZ_{cond}). While the properties of SAZ_{coal} were discussed in Efraim et al. (2022), the physical principle and the causes for SAZ_{cond} are presented in this study. A spectral-bin adiabatic parcel model was used to describe the effect of updraft (w) and different aerosol size distributions (ASD) on the existence and properties of SAZ_{cond}. The simulations showed that a stronger increase of w with decreasing T results in the change from unperturbed dominant condensational growth to the occurrence of SAZ_{cond} when a high-accelerated w increases S to the extent that it exceeds the maximum supersaturation simulated at the cloud base (S_{max}). This matches the results presented by Pinsky et al. (2012). The simulations also showed that, for the same w profile, a more polluted case with higher CCN concentrations and resulting lower S_{max} would lead to a SAZ_{cond} starting at lower cloud depths and with more significant activation of interstitial particles into cloud droplets. A method to detect SAZ_{cond} from T-r_e profiles measured by satellite was demonstrated using two case studies. One in which SAZ_{cond} was observed and another where it was not identified. We found that the existence of SAZ_{cond} may cause an overestimation of the satellite retrieved N_d due to: (a) the smaller r_e after SAZ_{cond} for the same amount of LWC_a, (b) the deviation from the assumption that all droplets were activated at cloud base, (c) the reduction of adiabaticity, and (d) the consideration of more adiabatic points with less certainty. In addition, SAZ_{cond} leads to a warm rain suppression and possible invigoration of the cloud by the released latent heat from ice nucleation above the 0 °C isotherm. The occurrence of *SAZ* has climatic importance by shaping the deep convective cloud microstructure with possible consequences for cloud radiative forcing. The ability to detect both SAZ_{cond} and SAZ_{coal} signatures from satellites allows a detailed analysis of convective cloud microphysics in large areas and over long periods. Further investigations and validations of these signatures in convective clouds will improve our understanding of their role in aerosol-cloud interactions.

Disclaimer

This paper contains results of research conducted under the Technical/Scientific Cooperation Agreement between the National Institute for Amazonian Research, the State University of Amazonas, and the Max-Planck-Gesellschaft e.V.; the opinions expressed are the entire responsibility of the authors and not of the participating institutions.

Financial support

This research has been supported by the BSF (grant no. 2020809), Max Planck Society, the Max Planck Graduate Center with the Johannes Gutenberg University Mainz (MPGC), the Bundesministerium für Bildung und Forschung (BMBF contracts 01LB1001A, 01LK1602B, and 01LK2101B), the Brazilian Ministério da Ciência, Tecnologia e Inovação (MCTI/FINEP contract 01.11.01248.00), the Conselho Nacional de Desenvolvimento Científico e Tecnológico (CNPq, Brazil) (process 200723/2015-4), the FAPESP (Fundação de Amparo à Pesquisa do Estado de São Paulo) (grant no. 2017/17047-0 and 2021/13610-8), the CNPq project (grant no. 169842/2017-7), and the CAPES project (grant no. 88887.368025/2019-00).

CRediT authorship contribution statement

Avichay Efraim: Conceptualization, Formal analysis, Investigation,

Methodology, Resources, Software, Visualization, Writing – original draft, Writing – review & editing. **Ramon C. Braga:** Conceptualization, Methodology, Resources, Writing – review & editing. **Daniel Rosenfeld:** Conceptualization, Methodology, Supervision, Writing – original draft. **Oliver Lauer:** Conceptualization, Formal analysis, Investigation, Methodology, Resources, Software, Writing – review & editing. **Marco A. Franco:** Methodology, Resources, Writing – review & editing. **Leslie A. Kremper:** Methodology, Resources, Writing – review & editing. **Christopher Pöhlker:** Writing – review & editing. **Meinrat O. Andreae:** Writing – review & editing. **Cléo Q. Dias-Junior:** Writing – review & editing. **Mira L. Pöhlker:** Conceptualization, Resources, Supervision, Writing – review & editing.

Declaration of Competing Interest

The authors declare that they have no known competing financial interests or personal relationships that could have appeared to influence the work reported in this paper.

Data availability

The satellite data of the case studies presented in this study is available on the VIIRS dataset found at the *NOAA's Comprehensive Large Array-data Stewardship System* [https://www.avl.class.noaa.gov/]. The ATTO data used in this study are available via the ATTO data portal at https://www.attoproject.org/. The output data from the IDL program of the sampled cloud scenes have been deposited in supplementary data files for use in follow-up studies [doi: https://doi.org/10.5061/dryad.h44j0zpnr]. For data requests beyond the available data, please refer to the corresponding author.

Acknowledgments

We thank the U.S.-Israel Binational Science Foundation (BSF) for financial support. In addtion, for the operation of the ATTO site, we acknowledge the support of the Max Planck Society, the German Federal Ministry of Education and Research and the Brazilian Ministério da Ciência, Tecnologia e Inovação as well as the Amazon State University (UEA), FAPEAM, LBA/INPA, and SDS/CEUC/RDS-Uatumã. We would like to especially thank all the people involved in the technical, logistical, and scientific support of the ATTO project. Thanks to Guy Pulik for his insightful observations and comments. Special thanks to Lior Efraim and Imri Yitzhak for their moral support.

Appendix A. Supplementary data

Supplementary data to this article can be found online at https://doi.org/10.1016/j.atmosres.2023.107196.

References

Anderson, N.F., Grainger, C.A., Stith, J.L., 2005. Characteristics of strong updrafts in precipitation systems over the Central Tropical Pacific Ocean and in the Amazon. J. Appl. Meteorol. 44 (5), 731–738. https://doi.org/10.1175/JAM2231.1.

Andreae, M.O., Acevedo, O.C., Araùjo, A., Artaxo, P., Barbosa, C.G.G., Barbosa, H.M.J., Brito, J., Carbone, S., Chi, X., Cintra, B.B.L., da Silva, N.F., Dias, N.L., Dias-Júnior, C. Q., Ditas, F., Ditz, R., Godoi, A.F.L., Godoi, R.H.M., Heimann, M., Hoffmann, T., Yáñez-Serrano, A.M., 2015. The Amazon Tall Tower Observatory (ATTO): overview of pilot measurements on ecosystem ecology, meteorology, trace gases, and aerosols. Atmos. Chem. Phys. 15 (18), 10723–10776. https://doi.org/10.5194/acp-15-10723-2015.

Andrejczuk, M., Grabowski, W.W., Malinowski, S.P., Smolarkiewicz, P.K., 2009. Numerical simulation of cloud–clear air interfacial mixing: homogeneous versus inhomogeneous mixing. J. Atmos. Sci. 66 (8), 2493–2500. https://doi.org/10.1175/2009JAS2956.1.

Arakawa, A., Schubert, W.H., 1974. Interaction of a Cumulus Cloud Ensemble with the Large-Scale Environment, Part I. J. Atmos Sci. 31 (3), 674–701. https://doi.org/10.1175/1520-0469(1974)031<0674:IOACCE>2.0.CO;2.

Baker, M.B., Corbin, R.G., Latham, J., 1980. The influence of entrainment on the evolution of cloud droplet spectra: I. A model of inhomogeneous mixing. Q. J. R. Meteorol. Soc. 106 (449), 581–598. https://doi.org/10.1002/qj.49710644914.

Beals, M.J., Fugal, J.P., Shaw, R.A., Lu, J., Spuler, S.M., Stith, J.L., 2015. Holographic measurements of inhomogeneous cloud mixing at the centimeter scale. Science 350 (6256), 87–90. https://doi.org/10.1126/science.aab0751.

Bera, S., Chowdhuri, S., Prabha, T.V., 2022. A new methodology for the statistical descriptions of particle-by-particle measurements of liquid droplets in cumulus clouds. Q. J. R. Meteorol. Soc. 148 (743), 842–859. https://doi.org/10.1002/qj.4234.

Bower, K.N., Choularton, T.W., 1988. The effects of entrainment on the growth of droplets in continental cumulus clouds. Q. J. R. Meteorol. Soc. 114 (484), 1411–1434. https://doi.org/10.1002/qj.49711448404.

Braga, R.C., Rosenfeld, D., Weigel, R., Jurkat, T., Andreae, M.O., Wendisch, M., et al., 2017. Further evidence for CCN aerosol concentrations determining the height of warm rain and ice initiation in convective clouds over the Amazon basin. Atmos. Chem. Phys. 17 (23), 14433–14456. https://doi.org/10.5194/acp-17-14433-2017.

Braga, R.C., Rosenfeld, D., Krüger, O.O., Ervens, B., Holanda, B.A., Wendisch, M., et al., 2021. Linear relationship between effective radius and precipitation water content near the top of convective clouds: measurement results from ACRIDICON–CHUVA campaign. Atmos. Chem. Phys. 21 (18), 14079–14088. https://doi.org/10.5194/acp-21-14079-2021.

Brenguier, J.-L., 1993. Observations of cloud microstructure at the centimeter scale. J. Appl. Meteorol. Climatol. 32 (4), 783–793.

Brenguier, J.-L., Pawlowska, H., Schüller, L., Preusker, R., Fischer, J., Fouquart, Y., 2000. Radiative properties of boundary layer clouds: Droplet effective radius versus number concentration. J. Atmos. Sci. 57 (6), 803–821.

Bréon, F.M., Tanré, D., Generoso, S., 2002. Aerosol effect on cloud droplet size monitored from satellite. Science 295 (5556), 834–838. https://doi.org/10.1126/science.1066434.

Burnet, F., Brenguier, J.-L., 2007. Observational study of the entrainment-mixing process in warm convective clouds. J. Atmos. Sci. 64 (6), 1995–2011. https://doi.org/10.1175/JAS3928.1.

Chen, R., Wood, R., Li, Z., Ferraro, R., Chang, F.-L., 2008. Studying the vertical variation of cloud droplet effective radius using ship and space-borne remote sensing data. J. Geophys. Res. 113, D00A02. https://doi.org/10.1029/2007JD009596.

Cotton, W.R., Bryan, G., van den Heever, S.C., 2011. The mesoscale structure of extratropical cyclones and middle and high clouds. In: International Geophysics, vol. 99. Elsevier, pp. 527–672. https://doi.org/10.1016/S0074-6142(10)09916-X.

Davis, A.B., Marshak, A., 2010. Solar radiation transport in the cloudy atmosphere: a 3D perspective on observations and climate impacts. Rep. Prog. Phys. 73 (2), 026801 https://doi.org/10.1088/0034-4885/73/2/026801.

Devenish, B.J., Bartello, P., Brenguier, J.-L., Collins, L.R., Grabowski, W.W., IJzermans, R.H.A., Malinowski, S.P., Reeks, M.W., Vassilicos, J.C., Wang, L.-P., Warhaft, Z., 2012. Droplet growth in warm turbulent clouds. Q. J. R. Meteorol. Soc. 138 (667), 1401–1429. https://doi.org/10.1002/qj.1897.

Efraim, A., Lauer, O., Rosenfeld, D., Braga, R.C., Franco, M.A., Kremper, L.A., et al., 2022. Satellite-based detection of secondary droplet activation in convective clouds. J. Geophys. Res. Atmos. 127 (12) https://doi.org/10.1029/2022JD036519.

Efraim, A., Rosenfeld, D., Schmale, J., Zhu, Y., 2020. Satellite Retrieval of Cloud Condensation Nuclei Concentrations in Marine Stratocumulus by Using Clouds as CCN Chambers. Journal of Geophysical Research: Atmospheres 125 (16). https://doi.org/10.1029/2020JD032409 e2020JD032409.

Fan, J., Leung, L.R., Rosenfeld, D., Chen, Q., Li, Z., Zhang, J., Yan, H., 2013. Microphysical effects determine macrophysical response for aerosol impacts on deep convective clouds. Proc. Natl. Acad. Sci. 110 (48), E4581–E4590. https://doi.org/10.1073/pnas.1316830110.

Fan, J., Rosenfeld, D., Zhang, Y., Giangrande, S.E., Li, Z., Machado, L.A.T., et al., 2018. Substantial convection and precipitation enhancements by ultrafine aerosol particles. Science 359 (6374), 411–418. https://doi.org/10.1126/science.aan8461.

Franco, M.A., Ditas, F., Kremper, L.A., Machado, L.A.T., Andreae, M.O., Araújo, A., et al., 2022. Occurrence and growth of sub-50 nm aerosol particles in the Amazonian boundary layer. Atmos. Chem. Phys. 22 (5), 3469–3492. https://doi.org/10.5194/acp-22-3469-2022.

Freud, E., Rosenfeld, D., 2012. Linear relation between convective cloud drop number concentration and depth for rain initiation: drop concentration and rain initiation. J. Geophys. Res. Atmos. 117 (D2) https://doi.org/10.1029/2011JD016457 n/a-n/a.

Freud, E., Rosenfeld, D., Andreae, M.O., Costa, A.A., Artaxo, P., 2008. Robust relations between CCN and the vertical evolution of cloud drop size distribution in deep convective clouds. Atmos. Chem. Phys. 8 (6), 1661–1675. https://doi.org/10.5194/acp-8-1661-2008.

Freud, E., Rosenfeld, D., Kulkarni, J.R., 2011. Resolving both entrainment-mixing and number of activated CCN in deep convective clouds. Atmos. Chem. Phys. 11 (24), 12887–12900. https://doi.org/10.5194/acp-11-12887-2011.

Gerber, H., 1996. Microphysics of marine Stratocumulus clouds with two drizzle modes. J. Atmos. Sci. 53 (12), 1649–1662. https://doi.org/10.1175/1520-0469(1996)053<1649:MOMSCW>2.0.CO;2.

Giangrande, S.E., Toto, T., Jensen, M.P., Bartholomew, M.J., Feng, Z., Protat, A., Williams, C.R., Schumacher, C., Machado, L., 2016. Convective cloud vertical velocity and mass-flux characteristics from radar wind profiler observations during GoAmazon2014/5. J. Geophys. Res. Atmos. 121 (21) https://doi.org/10.1002/2016JD025303.

Grosvenor, D.P., Wood, R., 2014. The effect of solar zenith angle on MODIS cloud optical and microphysical retrievals within marine liquid water clouds. Atmos. Chem. Phys. 14 (14), 7291–7321. https://doi.org/10.5194/acp-14-7291-2014.

Grosvenor, D.P., Sourdeval, O., Zuidema, P., Ackerman, A., Alexandrov, M.D., Bennartz, R., et al., 2018. Remote sensing of droplet number concentration in warm clouds: a review of the current state of knowledge and perspectives. Rev. Geophys. 56 (2), 409–453. https://doi.org/10.1029/2017RG000593.

Hill, T.A., Choularton, T.W., 1985. An airborne study of the microphysical structure of cumulus clouds: microphysical structure of cumulus clouds. Q. J. R. Meteorol. Soc. 111 (468), 517–544. https://doi.org/10.1002/qj.49711146813.

Hoppel, W.A., Frick, G.M., 1986. Ion—aerosol attachment coefficients and the steady-state charge distribution on aerosols in a bipolar ion environment. Aerosol Sci. Technol. 5 (1), 1–21. https://doi.org/10.1080/02786828608959073.

Huang, T., Zhu, Y., Rosenfeld, D., Yang, Y., Lam, D.H.Y., Leung, W.H., Lee, H.F., Cheng, J.C.H., Yim, S.H.L., 2022. Regime-dependent impacts of aerosol particles and updrafts on the cloud condensation nuclei and the enhanced warm rain suppression: evidence from synergistic satellite and LiDAR observations. Geophys. Res. Lett. 49 (3) https://doi.org/10.1029/2021GL097315.

Hudson, J.G., Noble, S., Tabor, S., 2015. Cloud supersaturations from CCN spectra Hoppel minima. J. Geophys. Res. Atmos. 120 (8), 3436–3452. https://doi.org/10.1002/2014JD022669.

IPCC, 2013. Summary for policymakers. In: Stocker, T.F., Qin, D., Plattner, G.-K., Tignor, M., Allen, S.K., Boschung, J., Nauels, A., Xia, Y., Bex, V., Midgley, P.M. (Eds.), Climate Change 2013: The Physical Science Basis. Contribution of Working Group I to the Fifth Assessment Report of the Intergovernmental Panel on Climate Change. Cambridge University Press, Cambridge, United Kingdom and New York, NY, USA, pp. 1–30. https://doi.org/10.1017/CBO9781107415324.004.

IPCC, 2021. Summary for policymakers. In: MassonDelmotte, V., Zhai, P., Pirani, A., Connors, S.L., Péan, C., Berger, S., Caud, N., Chen, Y., Goldfarb, L., Gomis, M.I., Huang, M., Leitzell, K., Lonnoy, E., Matthews, J.B.R., Maycock, T.K., Waterfield, T., Yelekçi, O., Yu, R., Zhou, B. (Eds.), Climate Change 2021: The Physical Science Basis. Contribution of Working Group I to the Sixth Assessment Report of the Intergovernmental Panel on Climate Change. Cambridge University Press, Cambridge, United Kingdom and New York, NY, USA, pp. 3–32. https://doi.org/10.1017/9781009157896.001.

Khain, A.P., Phillips, V., Benmoshe, N., Pokrovsky, A., 2012. The role of small soluble aerosols in the microphysics of deep maritime clouds. J. Atmos. Sci. 69 (9), 2787–2807. https://doi.org/10.1175/2011JAS3649.1.

King, N.J., Bower, K.N., Crosier, J., Crawford, I., 2013. Evaluating MODIS cloud retrievals with in situ observations from VOCALS-REx. Atmos. Chem. Phys. 13 (1), 191–209. https://doi.org/10.5194/acp-13-191-2013.

Köhler, H., 1936. The nucleus in and the growth of hygroscopic droplets. Trans. Faraday Soc. 32 (0), 1152–1161. https://doi.org/10.1039/TF9363201152.

Konwar, M., Maheskumar, R.S., Kulkarni, J.R., Freud, E., Goswami, B.N., Rosenfeld, D., 2012. Aerosol control on depth of warm rain in convective clouds: aerosol control on depth of warm rain. J. Geophys. Res. Atmos. 117 (D13) https://doi.org/10.1029/2012JD017585 n/a-n/a.

Kumar, B., Janetzko, F., Schumacher, J., Shaw, R.A., 2012. Extreme responses of a coupled scalar–particle system during turbulent mixing. New J. Phys. 14 (11), 115020 https://doi.org/10.1088/1367-2630/14/11/115020.

Latham, J., Reed, R.L., 1977. Laboratory studies of the effects of mixing on the evolution of cloud droplet spectra. Q. J. R. Meteorol. Soc. 103 (436), 297–306. https://doi.org/10.1002/qj.49710343607.

Lensky, I.M., Rosenfeld, D., 2006. The time-space exchangeability of satellite retrieved relations between cloud top temperature and particle effective radius. Atmos. Chem. Phys. 6 (10), 2887–2894. https://doi.org/10.5194/acp-6-2887-2006.

Lensky, I.M., Rosenfeld, D., 2008. Clouds-Aerosols-Precipitation Satellite Analysis Tool (CAPSAT). Atmos. Chem. Phys. 8 (22), 6739–6753. https://doi.org/10.5194/acp-8-6739-2008.

Marinescu, P.J., Kennedy, P.C., Bell, M.M., Drager, A.J., Grant, L.D., Freeman, S.W., Van Den Heever, S.C., 2020. Updraft vertical velocity observations and uncertainties in high plains supercells using radiosondes and radars. Mon. Weather Rev. 148 (11), 4435–4452. https://doi.org/10.1175/MWR-D-20-0071.1.

Marshak, A., Davis, A. (Eds.), 2005. 3D Radiative Transfer in Cloudy Atmospheres. Springer-Verlag. https://doi.org/10.1007/3-540-28519-9.

Marshak, A., Platnick, S., Várnai, T., Wen, G., Cahalan, R.F., 2006. Impact of three-dimensional radiative effects on satellite retrievals of cloud droplet sizes. J. Geophys. Res. 111 (D9), D09207. https://doi.org/10.1029/2005JD006686.

Paluch, I.R., 1986. Mixing and the cloud droplet size spectrum: generalizations from the CCOPE data. J. Atmos. Sci. 43 (18), 1984–1993.

Paluch, I.R., Baumgardner, D.G., 1989. Entrainment and fine-scale mixing in a continental convective cloud. J. Atmos. Sci. 46 (2), 261–278. https://doi.org/10.1175/1520-0469(1989)046<0261:EAFSMI>2.0.CO;2.

Paluch, I.R., Knight, C.A., 1984. Mixing and the evolution of cloud droplet size spectra in a vigorous continental cumulus. J. Atmos. Sci. 41 (11), 1801–1815. https://doi.org/10.1175/1520-0469(1984)041<1801:MATEOC>2.0.CO;2.

Pan, Z., Rosenfeld, D., Zhu, Y., Mao, F., Gong, W., Zang, L., Lu, X., 2021. Observational quantification of aerosol invigoration for deep convective cloud lifecycle properties based on geostationary satellite. J. Geophys. Res. Atmos. 126 (9) https://doi.org/10.1029/2020JD034275.

Pinsky, M., Khain, A., 2002. Effects of in-cloud nucleation and turbulence on droplet spectrum formation in cumulus clouds. Q. J. R. Meteorol. Soc. 128 (580), 501–533. https://doi.org/10.1256/003590002321042072.

Pinsky, M., Khain, A., Mazin, I., Korolev, A., 2012. Analytical estimation of droplet concentration at cloud base. J. Geophys. Res. Atmos. 117 (D18) https://doi.org/10.1029/2012JD017753 n/a-n/a.

Pinsky, M., Khain, A., Korolev, A., Magaritz-Ronen, L., 2016. Theoretical investigation of mixing in warm clouds – part 2: homogeneous mixing. Atmos. Chem. Phys. 16 (14), 9255–9272. https://doi.org/10.5194/acp-16-9255-2016.

Pöhlker, M.L., Pöhlker, C., Ditas, F., Klimach, T., Hrabe de Angelis, I., Araújo, A., et al., 2016. Long-term observations of cloud condensation nuclei in the Amazon rain forest – part 1: aerosol size distribution, hygroscopicity, and new model parametrizations for CCN prediction. Atmos. Chem. Phys. 16 (24), 15709–15740. https://doi.org/10.5194/acp-16-15709-2016.

Pöhlker, M.L., Ditas, F., Saturno, J., Klimach, T., Hrabě de Angelis, I., Araùjo, A.C., et al., 2018. Long-term observations of cloud condensation nuclei over the Amazon rain forest – part 2: variability and characteristics of biomass burning, long-range transport, and pristine rain forest aerosols. Atmos. Chem. Phys. 18 (14), 10289–10331. https://doi.org/10.5194/acp-18-10289-2018.

Pöhlker, M.L., Zhang, M., Campos Braga, R., Krüger, O.O., Pöschl, U., Ervens, B., 2021. Aitken mode particles as CCN in aerosol- and updraft-sensitive regimes of cloud droplet formation. Atmos. Chem. Phys. 21 (15), 11723–11740. https://doi.org/10.5194/acp-21-11723-2021.

Prabha, T.V., Khain, A., Maheshkumar, R.S., Pandithurai, G., Kulkarni, J.R., Konwar, M., Goswami, B.N., 2011. Microphysics of premonsoon and monsoon clouds as seen from in situ measurements during the Cloud Aerosol Interaction and Precipitation Enhancement Experiment (CAIPEEX). J. Atmos. Sci. 68 (9), 1882–1901. https://doi.org/10.1175/2011JAS3707.1.

Price, C., 2000. Evidence for a link between global lightning activity and upper tropospheric water vapour. Nature 406 (6793), 290–293. https://doi.org/10.1038/35018543.

Rogers, R.R., Yau, M.K., 1996. A Short Course in Cloud Physics, 3. ed., reprint. Butterworth Heinemann.

Rosenfeld, D., 2007. New insights to cloud seeding for enhancing precipitation and for hail suppression. J. Weather Modif. 39 (1), 61–69.

Rosenfeld, D., 2018. Cloud-aerosol-precipitation interactions based of satellite retrieved vertical profiles of cloud microstructure. In: Remote Sensing of Aerosols, Clouds, and Precipitation. Elsevier, pp. 129–152. https://doi.org/10.1016/B978-0-12-810437-8.00006-2.

Rosenfeld, D., Gutman, G., 1994. Retrieving microphysical properties near the tops of potential rain clouds by multispectral analysis of AVHRR data. Atmos. Res. 34 (1–4), 259–283. https://doi.org/10.1016/0169-8095(94)90096-5.

Rosenfeld, D., Lensky, I.M., 1998. Satellite-based insights into precipitation formation processes in continental and maritime convective clouds. Bull. Am. Meteorol. Soc. 79 (11), 2457–2476. https://doi.org/10.1175/1520-0477(1998)079<2457:SBIIPF>2.0.CO;2.

Rosenfeld, D., Kaufman, Y.J., Koren, I., 2006. Switching cloud cover and dynamical regimes from open to closed Benard cells in response to the suppression of precipitation by aerosols. Atmos. Chem. Phys. 6 (9), 2503–2511. https://doi.org/10.5194/acp-6-2503-2006.

Rosenfeld, D., Lohmann, U., Raga, G.B., O'Dowd, C.D., Kulmala, M., Fuzzi, S., et al., 2008. Flood or drought: how do aerosols affect precipitation? Science 321 (5894), 1309–1313. https://doi.org/10.1126/science.1160606.

Rosenfeld, D., Cattani, E., Melani, S., Levizzani, V., 2004. Considerations on Daylight Operation of 1.6 versus 3.7-μm Channel on NOAA and Metop Satellites. Bull. Am. Meteorol. Soc. 85 (6), 873–882. https://doi.org/10.1175/BAMS-85-6-873.

Rosenfeld, D., Fischman, B., Zheng, Y., Goren, T., Giguzin, D., 2014a. Combined satellite and radar retrievals of drop concentration and CCN at convective cloud base: Rosenfeld et. al.; retrieving convective cloud base CCN. Geophys. Res. Lett. 41 (9), 3259–3265. https://doi.org/10.1002/2014GL059453.

Rosenfeld, D., Liu, G., Yu, X., Zhu, Y., Dai, J., Xu, X., Yue, Z., 2014b. High-resolution (375 m) cloud microstructure as seen from the NPP/VIIRS satellite imager. Atmos. Chem. Phys. 14 (5), 2479–2496. https://doi.org/10.5194/acp-14-2479-2014.

Rosenfeld, D., Zheng, Y., Hashimshoni, E., Pöhlker, M.L., Jefferson, A., Pöhlker, C., et al., 2016. Satellite retrieval of cloud condensation nuclei concentrations by using clouds as CCN chambers. Proc. Natl. Acad. Sci. 113 (21), 5828–5834. https://doi.org/10.1073/pnas.1514044113.

Sayer, A.M., Govaerts, Y., Kolmonen, P., Lipponen, A., Luffarelli, M., Mielonen, T., Patadia, F., Popp, T., Povey, A.C., Stebel, K., Witek, M.L., 2020. A review and framework for the evaluation of pixel-level uncertainty estimates in satellite aerosol remote sensing. Atmos. Meas. Tech. 13 (2), 373–404. https://doi.org/10.5194/amt-13-373-2020.

Slingo, A., Slingo, J.M., 1988. The response of a general circulation model to cloud longwave radiative forcing. I: introduction and initial experiments. Q. J. R. Meteorol. Soc. 114 (482), 1027–1062. https://doi.org/10.1002/qj.49711448209.

Stephens, G.L., Tsay, S.-C., Stackhouse, P.W., Flatau, P.J., 1990. The relevance of the microphysical and radiative properties of cirrus clouds to climate and climatic feedback. J. Atmos. Sci. 47 (14), 1742–1754. https://doi.org/10.1175/1520-0469(1990)047<1742:TROTMA>2.0.CO;2.

Twomey, S., 1959. The nuclei of natural cloud formation part I: the chemical diffusion method and its application to atmospheric nuclei. Geofis. Appl. 43 (1), 227–242. https://doi.org/10.1007/BF01993559.

VanZanten, M., Stevens, B., Vali, G., Lenschow, D., 2005. Observations of drizzle in nocturnal marine stratocumulus. J. Atmos. Sci. 62 (1), 88–106.

Warner, J., 1969. The microstructure of cumulus cloud. Part I. General features of the droplet spectrum. J. Atmos. Sci. 26 (5), 1049–1059. https://doi.org/10.1175/1520-0469(1969)026<1049:TMOCCP>2.0.CO;2.

Warner, J., 1973. The microstructure of cumulus cloud: Part IV. The effect on the droplet spectrum of mixing between cloud and environment. J. Atmos. Sci. 30 (2), 256–261. https://doi.org/10.1175/1520-0469(1973)030%3C0256:TMOCCP%3E2.0.CO;2.

Wendisch, M., Pöschl, U., Andreae, M.O., Machado, L.A.T., Albrecht, R., Schlager, H., et al., 2016. ACRIDICON–CHUVA Campaign: studying tropical deep convective clouds and precipitation over Amazonia using the new German research aircraft HALO. Bull. Am. Meteorol. Soc. 97 (10), 1885–1908. https://doi.org/10.1175/BAMS-D-14-00255.1.

Yang, Y., Zhao, C., Wang, Y., Zhao, X., Sun, W., Yang, J., Ma, Z., Fan, H., 2021. Multi-source data based investigation of aerosol-cloud interaction over the North China Plain and North of the Yangtze Plain. J. Geophys. Res. Atmos. 126 (19), e2021JD035609 https://doi.org/10.1029/2021JD035609.

Yue, Z., Rosenfeld, D., Liu, G., Dai, J., Yu, X., Zhu, Y., Hashimshoni, E., Xu, X., Hui, Y., Lauer, O., 2019. Automated Mapping of Convective Clouds (AMCC) thermodynamical, microphysical, and CCN properties from SNPP/VIIRS satellite data. J. Appl. Meteorol. Climatol. 58 (4), 887–902. https://doi.org/10.1175/JAMC-D-18-0144.1.

Zhang, Z., Platnick, S., 2011. An assessment of differences between cloud effective particle radius retrievals for marine water clouds from three MODIS spectral bands. J. Geophys. Res. 116 (D20), D20215. https://doi.org/10.1029/2011JD016216.

Zhang, Z., Ackerman, A.S., Feingold, G., Platnick, S., Pincus, R., Xue, H., 2012. Effects of cloud horizontal inhomogeneity and drizzle on remote sensing of cloud droplet effective radius: case studies based on large-eddy simulations: heterogeneity and drizzle effect on effective radius retrieval. J. Geophys. Res. Atmos. 117 (D19) https://doi.org/10.1029/2012JD017655 n/a-n/a.

Zhao, C., Xie, S., Klein, S.A., Protat, A., Shupe, M.D., McFarlane, S.A., Comstock, J.M., Delanoë, J., Deng, M., Dunn, M., Hogan, R.J., Huang, D., Jensen, M.P., Mace, G.G., McCoy, R., O'Connor, E.J., Turner, D.D., Wang, Z., 2012. Toward understanding of differences in current cloud retrievals of ARM ground-based measurements. J. Geophys. Res. Atmos. 117 (D10) https://doi.org/10.1029/2011JD016792, 2011JD016792.

Zheng, Y., Rosenfeld, D., 2015. Linear relation between convective cloud base height and updrafts and application to satellite retrievals: satellite retrieval of cloud updrafts. Geophys. Res. Lett. 42 (15), 6485–6491. https://doi.org/10.1002/2015GL064809.

Zhu, Y., Rosenfeld, D., Yu, X., Liu, G., Dai, J., Xu, X., 2014. Satellite retrieval of convective cloud base temperature based on the NPP/VIIRS Imager. Geophys. Res. Lett. 41 (4), 1308–1313. https://doi.org/10.1002/2013GL058970.